Inverse Energy Cascade and the Upscale Cellular Growth of Stratocumulus Clouds

Florent Brient[1,2], **Basile Poujol**[1,3]

[1]Laboratoire de Météorologie Dynamique (LMD/IPSL), Sorbonne Université, CNRS, Paris, France
[2]Institut Universitaire de France, Paris, France
[3]Lycée Baimbridge, Les Abymes, Guadeloupe, France

Corresponding author, florent.brient@lmd.ipsl.fr

This manuscript is a non-peer-reviewed preprint submitted to EarthArXiv.

It has been submitted to *Quarterly Journal of the Royal Meteorological Society* for publication and not yet been peer reviewed. If accepted, the final version will be available viathe "Peer-reviewed Publication DOI" link on the right-hand side of this webpage. Please feel free to contact the corresponding author.

Version of 10 November 2026.

Inverse Energy Cascade and the Upscale Cellular Growth of Stratocumulus Clouds

Florent Brient[1,2], **Basile Poujol**[1,3]

[1]Laboratoire de Météorologie Dynamique (LMD/IPSL), Sorbonne Université, CNRS, Paris, France
[2]Institut Universitaire de France, Paris, France
[3]Lycée Baimbridge, Les Abymes, Guadeloupe, France

Last update : November 10, 2026

Key Points:

- Large-eddy simulations of marine stratocumulus show cells growing until an equilibrium aspect ratio of about 25-30 after about 20 hours.
- An inverse cascade transfer energy from small-scale vertical thermals to the large-scale horizontal field.
- Upscale growth resembles superstructures in Rayleigh–Bénard convection, suggesting a key role of kinetic energy transfers.

Corresponding author: Florent Brient, florent.brient@lmd.ipsl.fr

Abstract

Stratocumulus clouds are shallow convective clouds that exhibit mesoscale cellular organisation, with cell sizes of about 25–30 times the boundary-layer depth. Yet the physical processes controlling this large and robust aspect ratio remain unclear. Here we investigate this question using large-eddy simulations (LES) that reproduce the diurnal cycle of marine stratocumulus.

The simulations show an upscale growth of the cellular organisation at a rate of about one boundary-layer depth per hour ($\approx$+1 h^{-1}), until an equilibrium consistent with observations is reached. To analyse energy transfers across scales, we apply a turbulent energy cascade methodology to the 3D wind field. We find an inverse cascade of turbulent kinetic energy, transferring energy from small-scale vertical thermals, constrained by the boundary-layer depth, to large-scale horizontal structures. This cross-advection transfer acts mostly at night, when the boundary layer is coupled to the surface; during the day, decoupling gives rise to an isotropic horizontal–horizontal inverse cascade that also contributes to the mesoscale organisation. Additionally, the cells also feed a forward cascade, transferring their energy horizontally from the cell scale to smaller scales.

These results suggest that the upscale growth of cells in the stratocumulus-topped boundary layer is more consistent with a control by kinetic energy transfers and by stratification at the surface and cloud top than by humidity–radiation interactions. These findings are consistent with recent studies of superstructures in Rayleigh–Bénard convection simulations. Future work should now focus on the links between such dry superstructures and mesoscale organisation of atmospheric boundary layers, and on plume-plume and plume-environment interactions.

1 Introduction

Stratocumulus-topped boundary layers are low-level clouds that mostly occur over the subtropical ocean basins, either under strong atmospheric subsidence and ocean upwelling currents, or over the subsiding branches of extratropical cyclones [*Wood*, 2012]. Stratocumulus clouds form where a vertical temperature contrast exists between a cold surface and a temperature inversion at the boundary-layer top. While subsidence plays an important role in forming stratocumulus in baroclinic systems, it is mostly boundary-layer-top radiative cooling that maintains subtropical stratocumulus, by driving coherent downward plumes (downdrafts) that homogenize the mixed cloud layer together with surface-based coherent updrafts [*Brient et al.*, 2024].

Stratocumulus-topped boundary layers are characterized by condensate within the mixed boundary layer itself, in contrast to cumuliform clouds, which form in a stable layer above a dry, well-mixed subcloud layer. Stratocumulus also extend over very large horizontal areas while remaining constrained in boundary-layer depth, typically 0.5–3 km. In the South-East Pacific, the most extensive stratocumulus region, low clouds cover horizontal distances of order 3000 km, implying a domain-scale aspect ratio of Γ_{domain} ~1000–3000. Within this large-scale extent, clouds organize into a cellular pattern that has been clearly visible since the earliest satellite observations [*Krueger and Fritz*, 1961]. Individual cell size tends to increase with surface temperature and boundary-layer depth, and in fact scales remarkably well with boundary-layer depth: this yields a cellular aspect ratio Γ_{cell} ~25–30 that is close to constant across a wide range of conditions [*Wood and Hartmann*, 2006], albeit with a pronounced diurnal cycle [*Monnier et al.*, 2026]. To date, no consensus physical mechanism has been established to explain the growth, maintenance, and apparent universality of Γ_{cell}.

Under weaker large-scale subsidence and/or higher surface temperature, well-mixed stratocumulus-topped boundary layers tend to decouple, evolving into cumulus-under-stratocumulus configurations [*Rémillard et al.*, 2012] or open-cell stratocumulus [*Feingold et al.*, 2010], associated with conditional instability, wind shear, and/or precipitation [*Bretherton and Wyant*, 1997]. Interestingly, although closed and open cells lie at opposite ends of this transition, they exhibit similar spatial patterns [*Glassmeier and Feingold*, 2017]. Together with the broad diversity of mesoscale

cloud organization [*Stevens et al.*, 2020], this similarity motivates the search for common physical processes rather than regime-specific explanations.

Given their cellular structure, stratocumulus mesoscale organization is often compared to canonical Rayleigh–Bénard convection — natural convection driven by heating from below and cooling from above [*Ahlers et al.*, 2009]. The classical theory naturally produces cellular patterns with aspect ratios of order 1–3, but is not able to explain the much larger horizontal structures observed in stratocumulus (Γ_{cell} ~25–30). Relating atmospheric boundary layers to Rayleigh-Bénard convection was an active research topic in the late 20th century [*Agee et al.*, 1973; *Krishnamurti*, 1975; *Fiedler*, 1985; *Cieszelski*, 1998], but the absence of a physical theory extending Rayleigh-Bénard dynamics to these large-scale structures has since undermined the analogy [*Atkinson and Wu Zhang*, 1996].

More recently, however, Rayleigh-Bénard convection has offered new insight into how large-scale structures can grow, via the process of supergranule aggregation: the gradual clustering of small convective cells into large-scale structures, which can occur spontaneously in high-resolution Direct Numerical Simulations (DNS) of Rayleigh-Bénard convection [*Pandey et al.*, 2018; *Vieweg et al.*, 2021]. This aggregation is not generic, however, but requires a specific regime: high Rayleigh number, negligible background rotation, and Neumann boundary conditions at the surface (i.e., a prescribed vertical temperature gradient rather than a prescribed temperature) [*Green et al.*, 2020]. Under these conditions, the aggregation can be explained by an inverse cascade of kinetic energy and thermal variance, which transfers energy toward low wavenumbers (large scales) and sustains horizontally extended convection until growth saturates at the domain size [*Vieweg et al.*, 2022].

Strikingly, a similar upscale growth of cellular structures has also been reproduced with large-eddy simulations (LES) under realistic stratocumulus conditions [*de Roode et al.*, 2004; *Kazil et al.*, 2017; *Zhou and Bretherton*, 2019; *Ouyang et al.*, 2026] — but attributed to the opposite mechanism. There, upscale cell growth is explained by buoyancy forcing acting directly at the cell scale, which transfers energy downscale, explicitly ruling out an inverse-cascade interpretation. This is a genuine discrepancy between studies of superficially similar phenomena that invoke different physical explanations. Whether this reflects a real difference between dry Rayleigh-Bénard convection and moist, radiatively-forced stratocumulus, an artifact of differing numerical setups (DNS vs. LES, domain size, resolution), or an incomplete diagnosis of the energy cascade in one or both cases, remains unresolved.

In this study, we investigate the physical mechanisms driving the upscale growth of stratocumulus cells in large-eddy simulations, with the aim of clarifying this apparent contradiction. Building on the idea that stratocumulus cells behave analogously to supergranule aggregates of liquid water within the mixed boundary layer, we adopt a energy cascade framework to diagnose the direction and mechanisms of energy transfer governing cell growth. Because cellular patterns are also observed in other atmospheric configurations, such as the dry convective boundary layer [*Lareau et al.*, 2018], actiniform clouds [*Garay et al.*, 2004] or altocumulus [*Schmidt et al.*, 2013], we anticipate that the physical drivers identified here may extend beyond stratocumulus to the spatial organization of shallow atmospheric layers more broadly.

The remainder of this article is organized as follows. Section 2 describes the large-eddy simulations used to model the mesoscale organization of stratocumulus. The scale-to-scale energy cascade methodology is presented on section 3 and applied at different altitudes on section 4. Section 5 describes how the three-dimensional wind field helps understand the temporal growth of cells. Section 6 discusses the physical interpretation of our results in light of the DNS/LES discrepancy identified above, and Section 7 concludes.

2 Large-eddy simulation of stratocumulus

2.1 The setup

Stratocumulus clouds are represented following the setup of the European Project on Cloud Systems (EUROCS) First ISCCP Regional Experiment (FIRE) model intercomparison study [*Duynkerke et al.*, 2004], using the non-hydrostatic Meso-NH model v5.7.0 [*Lac et al.*, 2018]. The setup reproduces the meteorological conditions associated with the persistent cloud layer observed during the FIRE-I field campaign off the coast of California. Sea surface temperature and specific humidity are set to the intercomparison values (16°C and 11 g/kg, respectively), as are the initial vertical profiles of liquid-water potential temperature (θ_l) and total water mixing ratio (q_t), which feature a strong inversion near 600 m altitude ($\Delta\theta_l \approx 12$ K, $\Delta q_t \approx -3$ g/kg). Horizontal winds are set to constant geostrophic values (u=3.4 m/s, v=−4.9 m/s). Large-scale vertical velocity (-0.012 m/s at model top) and large-scale humidity and temperature forcings are taken from the intercomparison setup, yet with slight modification to allow stable long-term integration.

Reproducing large-aspect-ratio cellular patterns requires a sufficiently large domain [*de Roode et al.*, 2004]. Since investigating both the long-term upscale growth and the fine-scale physical mechanisms driving it requires, respectively, a large domain and a fine resolution, we define two complementary configurations:

- A low-resolution (LR) simulation over a domain of 90 km × 90 km with 300 m horizontal grid spacing, giving a domain aspect ratio $\Gamma_{\text{domain}} \approx 150$.
- A high-resolution (HR) simulation over a domain of 25.6 km × 25.6 km with 50 m horizontal grid spacing, giving $\Gamma_{\text{domain}} \approx 42$.

The vertical grid spacing is 10 m throughout the boundary layer, refined to 5 m across the inversion (560–620 m), and coarsened progressively to 500 m near the domain top (z = 4000 m), with 97 vertical levels in total. All analysis use a rescaled vertical grid with homogeneous 10 m grid spacing. Both simulations use periodic lateral boundary conditions and a time step of 1 s with the 1.5-order TKE subgrid turbulence scheme. The water phase transformation is simulated with a two-moment warm microphysics parametrization [*Geoffroy et al.*, 2010; *Khairoutdinov and Kogan*, 2000]. The LR simulation is run for 4 days to reach a statistically steady boundary layer (after 2 days). As the HR simulation is used specifically to analyze the upscale cellular growth, it is only run for 1 day.

Surface buoyancy fluxes are computed at each time step using a bulk aerodynamic formula [*Masson et al.*, 2013], and clear-sky and cloudy radiative fluxes are computed interactively using the ECMWF radiation scheme [*Gregory et al.*, 2000]. The simulation thus has fully interactive surface and radiative heat fluxes at its boundaries. Rain formation is switched off throughout.

2.2 Simulation of Stratocumulus

Figure 1 shows liquid water content and liquid water path (mean value and variance) for the long-term LR simulation. The simulated stratocumulus-topped boundary layer remains confined within the lowest 600 m of the atmosphere and exhibits a clear diurnal cycle in domain-averaged cloud liquid water content. Around sunrise (approximately 06:00 local time), solar absorption within the cloud layer reduces cloud-top radiative cooling and the associated in-cloud buoyancy production, weakening turbulent mixing and promoting decoupling with a stable layer near cloud base. This suppresses moisture transport from the surface layer into the cloud layer, raising the cloud-base height by approximately 100 m and reducing the domain-mean liquid water path (LWP) by approximately 67% relative to its nighttime value. Liquid water content recovers through the afternoon and evening as solar heating weakens and cloud-top cooling resumes, reaching a nighttime maximum of approximately 0.23 kg/m^2. This diurnal cycle is consistent across the simulated days, indicating a statistically repeatable response rather than a transient adjustment.

While the domain-averaged LWP follows an approximately sinusoidal diurnal cycle, its spatial variance (σ^2) peaks during each daytime period, lagging the LWP minimum (i.e., maximum decoupling) by approximately 4 hours. The standard deviation σ falls to a comparatively low, roughly constant nighttime value of approximately $2{\cdot}10^{-2}$ kg/m^2, punctuated by a secondary, smaller maximum just before sunrise.

The spatial distribution of LWP corroborates this picture (Figure 2), showing both the daytime increase in domain-mean LWP and the associated increase in its spatial variance, driven primarily by a stronger reduction of liquid water content at cell edges relative to cell interiors. The same figure reveals a progressive increase in mean cell size over time. The cellular mesoscale organization has become visibly aligned with the mean wind direction (146° S/SE), producing roll-like features that are most pronounced during daytime periods of weaker vertical mixing. Figure 2 also shows the organisation of the thermal field and of the turbulent kinetic energy (anomalies of the vertical-averaged field). The thermal field – defined through the liquid-water potential temperature θ_l (θ in the rest of the article for simplification) – exhibits a continuous growth of its cellular organisation, closely following that of the LWP. In contrast, the organisation of the TKE is less clear-cut and strongly modulated by the diurnal cycle, with minimum values during daytime. The HR simulation displays the same behaviour as the LR simulation (not shown).

To situate this configuration relative to Rayleigh–Bénard convection studies, we estimate order-of-magnitude values of the Prandtl, Rayleigh and Nusselt numbers from their classical definitions:

$$\mathrm{Pr} = \frac{\nu}{\alpha}, \qquad \mathrm{Ra} = \frac{g\beta\,\Delta\theta_v\,\mathsf{H}^3}{\nu\alpha}, \qquad \mathrm{Nu} = \frac{Q_0\,\mathsf{H}}{K\,\Delta\theta_v}, \tag{1}$$

where ν its kinematic viscosity, α its thermal diffusivity, g is the gravitational acceleration, β the thermal expansion coefficient of air, K its thermal conductivity. The boundary-layer depth H is defined as the altitude of maximum gradient of $\overline{\theta}$ (approximately 560–580 m – see Figure. 1). The temperature scale $\Delta\theta_v$ is the difference between the mean virtual potential temperatures of the 50-m-deep layers located immediately above and below H. The forcing Q_0 is the net heat flux driving the convection, defined as the sum of the boundary-layer radiative cooling and the surface buoyancy flux, both expressed in W m^{-2}.

In a DNS, ν and α are the molecular coefficients and all scales down to the dissipative range are resolved. In an LES, the smallest scales are instead represented by a subgrid closure, whose effective eddy viscosity and diffusivity greatly exceed the molecular values and depend on the grid resolution. We therefore evaluate ν and α from Sutherland's law with molecular air properties. This makes Pr and Ra more comparable to the Rayleigh-Bénard literature, although they do not correspond to the eddy diffusivity acting in the simulation. With this choice, Pr remains close to 0.71 throughout the simulation, varying by less than 0.1 % (Fig. 3). The Rayleigh number is of order 10^{17} (between 1.2 and 2×10^{17}, typically around 1.5×10^{17}), which chaAdditionalyracterizes fully developed turbulent free convection, far beyond the range usually reached by DNS. The Nusselt number is of order 10^5 but is strongly modulated by the diurnal cycle of the boundary-layer radiative tendency (it changes sign with Q_0). These estimates are necessarily approximate. They are intended to situate our configuration relative to the Rayleigh-Bénard DNS regime rather than to establish a precise dynamical equivalence.

2.3 Mesoscale organisation

For a given 2D field $\phi(x, y)$ with periodic boundary conditions, the variance spectrum is used to decompose the total variance σ_ϕ^2 across horizontal scales:

$$\sigma_\phi^2 = \iint \mathcal{P}_\phi(k_x, k_y)\,\mathrm{d}k_x\,\mathrm{d}k_y, \qquad \mathcal{P}_\phi(k_x, k_y) = \frac{|\hat{\phi}(k_x, k_y)|^2}{\Delta k_x\,\Delta k_y}, \tag{2}$$

where $\hat{\phi}$ is the 2D discrete Fourier transform of ϕ (normalised by $N_x N_y$ so that Parseval's identity holds), $\Delta k_x = 2\pi/L_x$ and $\Delta k_y = 2\pi/L_y$ are the wavenumber increments set by the do-

main size (the integral being in practice a discrete sum), and $\mathcal{P}_\phi$ is the variance density per unit wavenumber area.

It is more convenient, however, to express the spectrum as a function of the single isotropic wavenumber

$$k_{xy} = \sqrt{k_x^2 + k_y^2}.$$

The 1D spectrum $P_\phi(k_{xy})$ is obtained by integrating $\mathcal{P}_\phi$ over the azimuthal angle α of the horizontal wavevector $\mathbf{k}_h = (k_x, k_y) = k_{xy}(\cos\alpha, \sin\alpha)$, i.e. along the circle of radius $k_{xy} = |\mathbf{k}_h|$ centred on the origin of the (k_x, k_y) plane (in practice, summed over annuli of width Δk_{xy}):

$$P_\phi(k_{xy}) = \int_0^{2\pi} \mathcal{P}_\phi(k_{xy}, \alpha)\, k_{xy}\, \mathrm{d}\alpha \qquad \sigma_\phi^2 \simeq \int_{k_{\min}}^{k_{\max}} P_\phi(k_{xy})\, \mathrm{d}k_{xy}. \tag{3}$$

$P_\phi(k_{xy})$ is computed between $k_{\min} = 2\pi/L$ ($L = L_x = L_y$) and $k_{\max} = \pi/\Delta x$, the Nyquist wavenumber.

Figure 4 shows the radial variance spectrum of LWP over the first 48 hours of the LR simulation, with variance increasingly concentrated at the lowest wavenumbers over time. We define the mesoscale cellular length scale λ_{LWP} as the length scale corresponding to the peak of the smoothed variance spectrum at each time step (i.e., $\lambda_{\mathrm{LWP}} = 2\pi/k_{\mathrm{peak}}$), and the corresponding aspect ratio as $\Gamma_{\mathrm{LWP}} = \lambda_{\mathrm{LWP}}/\mathsf{H}$. The LR simulation reaches peak values comparable to satellite-derived estimates (25-35) after approximately 20 hours (Figure 4).

The 4-day evolution confirms the upscale growth of the LWP cellular organisation (Figure 5), with Γ_{LWP} increasing at a rate of approximately +1.55 h^{-1} over the first 20 hours. Γ_{LWP} then plateaus just below 30. At the onset of the second and third day, LWP variance increases again and Γ_{LWP} rise to higher plateaus of approximately 35 and 40, which then remain roughly constant during ≈24h. Note that our simulations do not reproduce the downscale cellular organization that has been reported in observations [*Monnier et al.*, 2026]. While solar radiation appears to modulate LWP characteristics (Figure 2), the upscale growth itself begins spontaneously in our simulation and subsequently becomes mostly decoupled from the diurnal cycle.

Aspect ratios can similarly be computed for other vertically-averaged fields. Figure 5 shows aspect ratio of liquid-water potential temperature $\Gamma_{\theta\theta}$, turbulent kinetic energy Γ_{TKE}, and total humidity Γ_{qq}. While all agree on the significant increase in the first 16 hours, Γ_{TKE} decrease at nighttime to value of around 10 while Γ_{qq} follows well Γ_{LWP}. The aspect ratio of the thermal field however alters between Γ_{TKE} and Γ_{qq}.

Starting from the turbulent kinetic energy $e = \frac{1}{2}\,\overline{u'^2 + v'^2 + w'^2}$, we compute the horizontal and vertical spectral components separately, using (u', v') and w' respectively:

$$P_{eh}(k_{xy}) = \tfrac{1}{2}\left[P_u(k_{xy}) + P_v(k_{xy})\right], \tag{4}$$
$$P_{ev}(k_{xy}) = \tfrac{1}{2}\,P_w(k_{xy}), \tag{5}$$

such that $P_e(k_{xy}) = P_{eh}(k_{xy}) + P_{ev}(k_{xy})$ integrates to the total TKE, $\int P_e(k_{xy})\,\mathrm{d}k_{xy} = e$. Figure 5 shows the horizontal scale of kinetic energy variability is entirely set by the horizontal component, Γ_{eh}, which decreases sharply at night and strengthens during daytime to reach Γ_{LWP} estimates. At night, Γ_{eh} approaches the comparatively constant value of the vertical-TKE aspect ratio, $\Gamma_{ev} \approx 5$. The absence of upscale growth in the vertical-TKE aspect ratio suggests limited mesoscale organisation of vertical plumes at the scale of the LWP cells. Despite known diurnal mesoscale organisation of vertical plumes [*Brient et al.*, 2024], vertical energy input is more constrained at scales around 5H than at the cell size.

These results are consistent with the HR simulation (Figure 6), which exhibits qualitatively similar behaviour but with a slower upscale growth rate (+1.25 h^{-1}) and a lower saturated aspect ratio after 36 hours (Γ_{LWP} ≈25). The HR simulation shows an average value of Γ_{ev} of approximately 2.5, which is lower than that of the LR simulation, but with a more pronounced diurnal

cycle. As before, the spatial organization of the TKE field reflects the interplay between the small-scale organization of vertical plumes at nighttime and the mesoscale organization of liquid and thermal scalars at daytime.

As the HR simulation reproduces well features simulated in the LR simulation, we use the former to analyzing the cellular upscale growth in the following sections.

3 Energy cascade

In fluid flows, the non-linearity of the Navier-Stokes equations couples different scales of motion, allowing energy to be transferred between them. In this section, we propose to quantify these energy transfers in the simulation using the turbulent energy cascade theory.

The TKE budget can be expressed in Fourier space using Parseval's identity. Let $\hat{E}(\mathbf{k}, t)$ be the three-dimensional spectral TKE density in wavenumber space and $E(k, t)$ its shell-integrated counterpart, with $k = \|\mathbf{k}\|$ and Ω the direction of $\mathbf{k}$:

$$E(k,t) = k^2 \iint_{4\pi} \hat{E}(\mathbf{k}, t)\, \mathrm{d}^2\Omega, \tag{6}$$

such that $e(t) = \int_0^\infty E(k,t)\, \mathrm{d}k$ is the volume-averaged TKE. The simplified budget at scale k reads

$$\frac{\partial E(k,t)}{\partial t} = \epsilon_{\mathrm{inj}}(k,t) - \epsilon_{\mathrm{diss}}(k,t) - \widetilde{T}(k,t), \tag{7}$$

where the first two terms are injection and dissipation, and $\widetilde{T}$ is the nonlinear energy transfer across scales. This transfer is a flux divergence in Fourier space, which defines the spectral energy flux $\Pi(k,t)$ (in $\mathrm{m}^2\,\mathrm{s}^{-3}$):

$$\widetilde{T}(k,t) = k^2 \iint_{4\pi} \mathrm{Re}[\mathbf{T}_{\mathrm{NL}}(\mathbf{k},t) \cdot \hat{\mathbf{u}}^*(\mathbf{k},t)]\, \mathrm{d}^2\Omega = \frac{\partial \Pi(k,t)}{\partial k}. \tag{8}$$

with $\mathbf{T}_{\mathrm{NL}}$ the Fourier transform of the nonlinear advection term $(\mathbf{u} \cdot \nabla)\mathbf{u}$. Since the nonlinear term only redistributes energy, $\int_0^\infty \widetilde{T}\, \mathrm{d}k = 0$ and integrating Eq. (7) over k gives $\partial e/\partial t = \epsilon_{\mathrm{inj}} - \epsilon_{\mathrm{diss}}$. By convention, $\Pi(k) > 0$ corresponds to a net transfer of energy from large to small scales (direct cascade), and $\Pi(k) < 0$ to the reverse (inverse cascade).

Rather than evaluating $\Pi(k)$ via the Fourier-shell integral above, it is more practical in our setting to use the equivalent real-space, coarse-graining formulation [*Alexakis and Biferale*, 2018], in which the spectral flux is expressed as the rate of work done by the small-scale strain on the large-scale-filtered field:

$$\Pi(k,t) = \overline{\mathbf{u}_{<k}(\mathbf{r},t) \cdot [(\mathbf{u} \cdot \nabla)\mathbf{u}]}, \tag{9}$$

with $\overline{(\cdot)}$ denotes a spatial average over the domain at a given time t. The large-scale-filtered field $\mathbf{u}_{<k}$ retains only wavenumbers smaller than k:

$$\mathbf{u}_{<k}(\mathbf{r},t) = \iiint_{\|\boldsymbol{\kappa}\|<k} \hat{\mathbf{u}}(\boldsymbol{\kappa},t)\, e^{i\boldsymbol{\kappa}\cdot\mathbf{r}}\, \mathrm{d}^3\boldsymbol{\kappa}. \tag{10}$$

Here $\mathbf{u} = (u', v', w')$ is the resolved 3D wind field, and the sign convention chosen so that $\Pi > 0$ denotes a direct (downscale) cascade, consistent with the definition above. The cascade can also be calculated for other variables, such as the spectral thermal variance flux Π_θ defined as:

$$\Pi_\theta(k,t) = \overline{\theta_{<k}(\mathbf{r},t)\ [\mathbf{u} \cdot \nabla\theta]}, \tag{11}$$

with θ the liquid-water potential temperature. While useful for interpreting the evolution of the thermal field [e.g. *Vieweg et al.*, 2022], this study will mostly use it for comparison with Π.

From simple dimensional analysis, one can derive the expected form of the energy spectrum $E(k)$ in statistically stationary, homogeneous, isotropic turbulence [e.g. *Frisch*, 1995]. In the *inertial range* (scales smaller than the forcing scale but larger than the dissipation scale), the spectral flux is neither produced nor dissipated and is therefore constant, $\Pi(k) = \Pi_0$. Since the mean energy flux per unit mass Π_0 (m^2/s^3) can then depend only on wavenumber k (m^{-1}) and the spectrum $E(k)$ (m^3/s^2), dimensional analysis yields the classical *Kolmogorov* $-5/3$ *law*:

$$E(k) \propto \Pi_0^{2/3}\, k^{-5/3}.$$

Thus, although the cascade maintains a constant spectral flux, energy is not evenly distributed across scales but follows the $-5/3$ power law between the forcing and dissipation scales (as shown on figure 2). This scaling holds only in a statistically stationary regime, i.e., when the forcing timescale is long compared with the cascade timescale.

This picture, valid for 3D isotropic turbulence, breaks down when one spatial dimension is much smaller than the other two (high domain aspect ratio). In this quasi-two-dimensional limit, vortex stretching vanishes and vorticity becomes materially conserved following fluid parcels, giving rise to the distinct dynamics of 2D turbulence [*Kraichnan*, 1967; *Leith*, 1968; *Batchelor*, 1969]. Geophysical fluids can be viewed as an intermediate state, quasi-two-dimensional at scales larger than the boundary-layer depth H ($k < 2\pi/\mathsf{H}$) and three-dimensional at smaller scales ($k > 2\pi/\mathsf{H}$). This can result in a *split cascade*, with different cascade directions on either side of the energy injection scale [*Celani et al.*, 2010; *Alexakis and Biferale*, 2018; *Poujol et al.*, 2020]. Under those conditions, the forward cascade of enstrophy exhibits a -3 slope, while the inverse cascade of energy displays a $-5/3$ slope.

By extending over thousands of kilometers horizontally while remaining confined to a boundary-layer depth of 0.5–2 km, the stratocumulus-topped boundary layer is strongly anisotropic and thus a plausible candidate for such a split-cascade regime.

4 Application to 2D fields

In line with conventional atmospheric science practices, the cascade methodology is first applied to horizontal (2D) fields. blinded of information at the altitude above and below it, as would be done by turbulence monitoring and structures functions derived from flight transect [e.g. *Nowak et al.*, 2025] or Doppler Lidar data [e.g. *Zhou et al.*, 2025]. Therefore, the vertical gradients are not used in the calculation.

4.1 Budget of Turbulent Kinetic Energy

We begin by analyzing the TKE budget as a function of height. Starting from the Navier–Stokes equations under the Boussinesq approximation [*Stull*, 1988], and assuming horizontal homogeneity, the budget of the TKE $e(z)$ can be written as:

$$\frac{\partial e(z)}{\partial t} + \underbrace{\overline{w}\,\frac{\partial e(z)}{\partial z}}_{\text{Advection}} = \underbrace{-\overline{u'w'}\,\frac{\partial \overline{u}}{\partial z} - \overline{v'w'}\,\frac{\partial \overline{v}}{\partial z}}_{\text{Shear production}} + \underbrace{\frac{g}{\theta_{v0}}\,\overline{w'\theta_v'}}_{\text{Buoyancy production}} - \underbrace{\epsilon}_{\text{Dissipation}}$$
$$- \underbrace{\frac{\partial}{\partial z}\left(\tfrac{1}{2}\,\overline{w'\,u_i'u_i'}\right)}_{\text{Turbulent transport}} - \underbrace{\frac{\partial}{\partial z}\left(\frac{\overline{w'p'}}{\overline{\rho}}\right)}_{\text{Pressure transport}} + \underbrace{\mathcal{R}}_{\text{Residual}}. \tag{12}$$

with $\overline{(\cdot)}$ the horizontal average over the domain at height z, primes denote deviations from it. Further integration over z recovers $\partial e/\partial t = \epsilon_{\text{prod}} - \epsilon_{\text{diss}}$ with ϵ_{prod} being the production by shear and buoyancy. It is similar with the vertically-integrated of equation 7 with $\epsilon_{\text{inj}} = \epsilon_{\text{prod}}$.

Figure 7 shows the domain-averaged TKE budget terms at t=6h (nighttime) and t=12h (daytime). It highlights the dominance of resolved terms, and mostly buoyancy fluxes associated with

cloud formation. While pressure redistributes energy from the bulk of the layer toward its boundaries, nonlinear transport increases TKE in the middle of the boundary layer and decreases it near the boundaries ; this transport partly compensates the strong buoyancy-flux energy source near cloud top ($z \approx 0.9\,\mathsf{H}$). At daytime, boundary-layer decoupling can be shown with the negative buoyancy production between 100 and 250 m, yet with pressure redistribution becoming positive. Subgrid fluxes are relatively weak, yet with relatively strong loss by dissipation at the boundary-layer boundaries.

4.2 Horizontal energy transfers

In line with conventional atmospheric science practices, the cascade methodology is first applied to horizontal (2D) fields averaging over annuli rather than shells. At each altitude, energy spectra and cascades are calculated blinded of information at the altitude above and below it, as would be done by turbulence monitoring and structures functions derived from flight transect [e.g. *Nowak et al.*, 2025] or Doppler Lidar data [e.g. *Zhou et al.*, 2025]. Therefore, the vertical gradients are not used in the calculation.

Figures 8 and 9 show, respectively, the 2D spectra and the cascades of TKE and θ variance at different levels of the boundary layer, for the HR simulation at $t + 6$ h, when the cells grow upscale (Figure 6). Kinetic energy is maximum near the layer boundaries, with a peak at $k_\lambda = 2\pi/\lambda_{\mathrm{LWP}}$, whereas no clear peak is visible in the bulk. Thermal variance also peaks at the cell scale, but differs from TKE at high wavenumbers (small scales) where it shows stronger amplitude at cloud top and weaker in the bulk. This in line with differences in spatial fields of θ and TKE as already seen in figure 2.

Figure 9a reveals direct (downscale) energy cascades from the cell scale λ_{LWP} toward smaller scales in the lowest and highest parts of the boundary layer. The inertial range is found at wavenumbers around $k_{\mathsf{H}} = 2\pi/\mathsf{H}$, the wavenumber corresponding to the boundary-layer depth, and is confirmed by a $-5/3$ slope in the energy spectrum (Figure 8a). An inverse cascade appears in the bulk for $k < k_{\mathsf{H}}/2$, but it is relatively weak (an order of magnitude smaller than near the boundaries). In contrast, thermal variance shows significant direct cascades from the cell scale to the dissipation range at all altitudes (figure 9b).

To better visualize the gains and losses of energy, we compute the buoyancy flux, the pressure redistribution and the non-linear transfer terms in Fourier space from equation 12 at each altitude. Figure 10 shows that energy production peaks at the cell scale, driven both by positive buoyancy fluxes in the dry subcloud layer and by condensation heating (partly compensated by pressure redistribution at cloud base). Together, these results confirm the 2D cascade analysis: the energy injected by buoyancy at the cell scale is redistributed toward smaller scales near the layer boundaries. The non-linear transfer is weaker but shows an energy loss at the layer boundaries and a gain at cloud base.

In summary, using only 2D field, the direct (downscale) spectral energy transfer clearly dominates the weak inverse (upscale) transfer found at cloud base. Our results support the picture proposed by *Zhou and Bretherton* [2019], in which the horizontal cascade remains strictly direct at all resolved scales, and upscale growth arises instead from a progressive increase in the buoyancy-forcing injection scale itself — likely driven by radiative, thermodynamic, and moisture interactions operating at the cell scale [*Ouyang et al.*, 2026]. This is broadly consistent with other studies that highlight the role of radiation on shallow and deep convective organization in conditionally unstable, cloudy regimes [e.g. *Pauluis and Schumacher*, 2011; *Muller and Bony*, 2015; *Agasthya et al.*, 2025].

This 2D analysis, however, does not capture the vertical injection of energy by thermals operating at scales smaller than the mesoscale cell size; we address this limitation in Section 5 using the fully 3D wind field.

5 On the importance of using 3D fields

5.1 Full energy cascade

In contrast to classical 2D turbulence, where energy is injected horizontally through vortical motions, the stratocumulus-topped boundary layer has heat, moisture, and energy fluxes driven by coherent thermal plumes. These plumes may organize in space, merge, or be inhibited by decoupling effects, yet remain constrained by the boundary-layer height set by the strong density inversion. In convectively-driven atmospheric boundary layers, it is therefore particularly difficult to identify a single scale of energy injection.

To account for both small-scale vertical thermals and large-scale horizontal cells, we compute the energy spectrum and cascade in the full 3D space. Two caveats to this methodology are worth noting:

1. The model grid is highly anisotropic, with a horizontal resolution of 50 m (HR) and a vertical resolution varying between 5 and 10 m within the boundary layer. Despite interpolating the native vertical grid onto a homogeneous 10 m grid, this anisotropy persists in the resulting Fourier space.
2. The 3D Fourier transform assumes periodicity of the wind field at boundaries, which is exact only in the horizontal directions.

Starting back from methods explained on section 3, we compute the energy spectrum by summing over spherical shells of width dk in the 3D wavenumber space, using the isotropic wavenumber

$$k = \sqrt{k_x^2 + k_y^2 + k_z^2}.$$

Following *Alexakis et al.* [2024], we additionally decompose the 3D spectrum into horizontal (perpendicular) and vertical (parallel) components, $\Pi(k_h)$ and $\Pi(k_v)$, using $k_h = \sqrt{k_x^2 + k_y^2}$ and $k_v = |k_z|$. The horizontal spectrum is obtained by summing the spectral energy and transfer densities over all grid points sharing a given value of k_h, irrespective of k_z (i.e., a full cylindrical integration over the vertical wavenumber) using logarithmically-spaced bins in k_h. The vertical spectrum is obtained analogously by summing over all (k_x, k_y) at fixed k_z, using the native discrete vertical wavenumbers themselves as bin edges; as a result, the spectrum has a coarser and non-log-uniform resolution set directly by the number of vertical levels, which may provide a discretized appearance of the spectrum. For both decompositions we retain the shell/plane-integrated energy:

$$\Pi_h(k_h) = \int_0^{k_h} \widetilde{T}_h(k_h')\,\mathrm{d}k_h', \qquad \Pi_v(k_v) = \int_0^{k_v} \widetilde{T}_v(k_v')\,\mathrm{d}k_v', \tag{13}$$

consistent with the continuous definition $\partial\Pi/\partial k = \widetilde{T}(k)$ introduced in Section 3. As before, the residual oblique transfer $\Pi_{\text{oblique}}(k)$ (triads with k_x, k_y, k_z all nonzero) may be obtained from $\Pi(k) = \Pi(k_h) + \Pi(k_v) + \Pi_{\text{oblique}}(k)$, and is not computed directly.

Figure 11a shows the resulting energy spectra in the full 3D space at t+6h. Energy slowly decreases between the cell scale ($k = k_\lambda$) and the boundary-layer-depth scale ($k \approx 1.5\ k_\mathsf{H}$) following a slope close to $-5/3$. It then increases sharply (by roughly a factor of 10) and decreases toward small scales following a -3 slope. The mode decomposition helps interpret the full spectrum. The horizontal spectrum shows an clear energy maximum at the cell scale, a $-5/3$ slope at intermediate wavenumbers, and rapid decay for $k > 2\,k_\mathsf{H}$. It shows consistency with the 2D energy spectrum (Figure 8). The vertical spectrum peaks near k_H, the smallest vertical wavenumber set by the boundary-layer depth, and decreases following an approximate k^{-3} slope as does the full spectrum. At very high wavelengths, the vertical component dominates simply because it is the only one that exists; however, at all wavelengths where both components exist, it is the vertical component that is the most energetic. The decomposition thus help understand the full spectra, yet a non-negligible part of energy is tranferred through oblique wavenumbers ($k_x, k_y, k_z \neq 0$)

Figure 11b shows the corresponding energy cascades. The horizontal-mode cascade confirms the 2D result of section 3: energy injected at the cell scale is transferred strictly downscale. The vertical-mode cascade shows a direct transfer from k_H toward small scales, consistent with three-dimensional turbulence dynamics acting along the vertical direction. The full 3D cascade, however, reveals a qualitatively different behavior: while energy is transferred toward high wavenumbers for $k > k_\mathsf{H}$, an inverse cascade is observed from $k \approx 0.9\, k_\mathsf{H}$ ($l = 1.1\mathsf{H}$) to scales of $k \approx k_\mathsf{H}/10$ ($l = 0.1\mathsf{H} \approx \lambda_{\mathrm{LWP}}$).

Figure 12 shows the evolution in time of the integral of the *negative part* of the full turbulence cascade for wavenumbers lower than k_H (relative to the maximum value). The inverse cascade is present from the onset of the simulation and intensifies during the first 6 hours. Subsequently, it exhibits a distinct diurnal cycle, dropping to near-zero values at night, before a resurgence of the negative cascade emerges during the second night. It confirms the continuous large-scale transfer of energy, but also show that solar effects on the boundary layer act on reducing this cascade on average.

As explained above, one caveat of our method is the use of a 3D Fourier transform in a domain that is not periodic in the vertical. To address this, we also compute the kinetic energy cascade Π (equation 9) using scale filtering with periodic 2D FFTs in x and y and a Discrete Sine Transform (DST) in z. The DST respects the physical boundary condition ($w = 0$ at the bottom and top boundaries) instead of assuming full 3D periodicity. Figure 12 shows that this approach yields results qualitatively similar to the 3D FFT method, albeit with weaker absolute values. This suggests that the negative cascade is not an artifact of the vertical periodicity assumed in the 3D FFT.

We think that these results are central to reconciling the discrepancy raised in Section 1 between DNS studies reporting inverse-cascade-driven upscale growth [*Vieweg et al.*, 2021, 2022] and LES-based studies reporting purely downscale, buoyancy-driven growth [*Zhou and Bretherton*, 2019; *Ouyang et al.*, 2026]. We find that inverse energy transfer emerges only when wavevector triads involve a nonzero vertical wavenumber component ($k_z \neq 0$); the purely horizontal mode ($k_z = 0$) however transfers energy strictly downscale from the cell scale, as also shown by the 2D analysis of Section 3. This suggests that the apparent contradiction with previous studies may reflect a difference in dimensionality of the diagnostic used, rather than a fundamental difference in the underlying physics: horizontally-restricted cascade analyses cannot capture the vertically-mediated inverse-transfer channel identified here, which may explain why it was reported in fully 3D DNS studies but not in previous LES-based horizontal cascade analyses.

5.2 Cross-advection terms

To go further, we decompose the 3D energy cascade into self-advection and cross-advection contributions:

$$\Pi(k) = \Pi_{hh}(k) + \Pi_{vv}(k) + \Pi_{hv}(k) + \Pi_{vh}(k) \tag{14}$$

Consistent with the sign convention adopted in section 3, they are defined as:

$$\Pi_{hh}(k) = \overline{\mathbf{u}^h_{<k} \cdot \left(\mathbf{u}^h \cdot \nabla_h \mathbf{u}^h\right)} \qquad \Pi_{vv}(k) = \overline{w_{<k}\,(w\,\partial_z w)} \tag{15}$$

$$\Pi_{hv}(k) = \overline{\mathbf{u}^h_{<k} \cdot \left(w\,\partial_z \mathbf{u}^h\right)} \qquad \Pi_{vh}(k) = \overline{w_{<k}\left(\mathbf{u}^h \cdot \nabla_h w\right)} \tag{16}$$

with $\mathbf{u} = (\mathbf{u}^h, w)$. This decomposition follows directly from expanding $\mathbf{u}_{<k} \cdot (\mathbf{u} \cdot \nabla)\mathbf{u}$ by velocity component and is therefore exact.

The first two terms describe self-advection—the advection of the horizontal (respectively vertical) velocity field by itself—and the last two describe cross-advection, in which one velocity component advects the other. Specifically, Π_{hv} term represent the advection of the horizontal wind field by vertical motions, whereas Π_{vh} term, the advection of the vertical velocity field by horizontal motions.

Figure 13a shows the cascade separation at t+6h. All four terms are positive (direct cascade) for wavenumbers $k > k_{\mathsf{H}}$, and thus consistent with a direct, three-dimensional cascade in this range. For $k < k_{\mathsf{H}}$, the horizontal self-advection term Π_{hh} remains direct, indicating that horizontal advection alone continues to transfer energy downscale even at scales larger than the boundary-layer depth — consistent with section 3. The vertical self-advection term Π_{vv} is close to zero for $k \leq k_{\mathsf{H}}$, as expected physically: since w must vanish at the surface and at the boundary-layer top, the vertical velocity field carries negligible spectral energy at scales larger than H, leaving little for Π_{vv} to transfer there. The cross-advection terms show more structured behavior. The Π_{hv} term is predominantly negative (inverse cascade) for wavenumbers corresponding to scales between H and $2\mathsf{H}$. The Π_{vh} term is negative over a broader range, from $2\mathsf{H}$ up to the cell scale λ_{LWP}, and dominates the net inverse-cascade signal identified in the full 3D flux. It is worth noting that Π_{hh} and Π_{hv} mostly compensate each other.

Figure 14 shows the time evolution of the integrated cascades for $k < 0.9\,k_{\mathsf{H}}$. It confirms that the total inverse cascade is weaker during daytime (as already seen in figure 12) and may even change sign at that time of day. This daytime variation is mainly driven by the cross-advection term Π_{hv}, which suggests that the action of the vertical velocity on the horizontal field changes with solar radiation. By contrast, Π_{vh} is weaker but remains negative throughout the day, suggesting that cellular patterns consistently favour the aggregation of coherent vertical motions. The isotropic term Π_{hh} is mostly positive but changes sign during daytime, in anticorrelation with Π_{hv}. However, it is worth noting that while the negative Π_{hv} cascade is confined to relatively low wavenumbers ($0.4\,k_{\mathsf{H}} < k < 0.9\,k_{\mathsf{H}}$; see figure 13), the negative part of Π_{hh} extends to larger scales (typically between $0.4\,k_{\mathsf{H}}$ and k_λ - not shown). This may help explain why cellular patterns can continue growing during daytime (figure 6). A similar temporal variability is found in the LR simulation, although with a negligible Π_{vh} component (not shown).

We explain this variability through the diurnal cycle of the stratocumulus-topped boundary layer. At daytime, the boundary layer is decoupled and thermals can no longer coherently connect the surface and cloud-top boundaries. We hypothesize that this decoupling, driven by near-cloud-base stabilization, slow down vertical plumes, decrease mean TKE (Figure 2), and reduce their ability to transfer energy in large scales. At the same time, surface-based warm updrafts — no longer constrained by a continuous, vertically coupled return flow — merge with neighboring updrafts, and cloud-top downdrafts spread and organize independently. This create areas of convergence/divergence that transfers energy horizontally, which is able to reach the mesoscales we simulate. Further research is nevertheless needed to identify whether these inverse cascades are sufficient to explain by themselves the growth rate of the cells that reach values of 30–40 as reported in Section 2, or if other physical processes also play a significant (or even dominant) role in this growth.

5.3 Importance of boundaries

To identify the altitudes at which the cascade is most active, we compute the spectral energy flux from wind fields restricted to the layers below and above a cutoff altitude z, and follow its evolution as z increases from 0 to H. Let $\tilde{\mathbf{u}}(x, y, z')$ denote the resolved 3D wind field on $z' \in [0, H]$, and let $\mathcal{H}_z$ be the indicator function of the layer $[0, z]$:

$$\mathcal{H}_z(z') = \begin{cases} 1, & 0 \leq z' \leq z \\ 0, & z < z' \leq H. \end{cases} \tag{17}$$

We define the lower-layer and upper-layer wind fields as

$$\tilde{\mathbf{u}}_+(x, y, z'; z) = \mathbf{u}(x, y, z')\,\mathcal{H}_z(z'), \tag{18}$$

$$\tilde{\mathbf{u}}_-(x, y, z'; z) = \mathbf{u}(x, y, z')\,\left[1 - \mathcal{H}_z(z')\right], \tag{19}$$

so that $\tilde{\mathbf{u}}_+ + \tilde{\mathbf{u}}_- = \mathbf{u}$ by construction. The corresponding bottom-up and top-down truncated spectral energy fluxes are defined, following the sign convention of Eq. 9, as

$$\Pi_+(k,z) = \overline{\tilde{\mathbf{u}}_{+,<k} \cdot \big(\tilde{\mathbf{u}}_+ \cdot \nabla\big)\tilde{\mathbf{u}}_+} \tag{20}$$

$$\Pi_-(k,z) = \overline{\tilde{\mathbf{u}}_{-,<k} \cdot \big(\tilde{\mathbf{u}}_- \cdot \nabla\big)\tilde{\mathbf{u}}_-} \tag{21}$$

where $(\cdot)$ denotes the volume average over the full domain $[0, H]$, and $\tilde{\mathbf{u}}_{\pm,<k}$ is the large-scale-filtered truncated field, defined analogously to Eq. 10 with 3D Fourier transform. By construction, $\Pi_+(k,0) = \Pi_-(k,H) = 0$ and $\Pi_+(k,H) = \Pi_-(k,0) = \Pi(k)$, the full-domain flux of Eq. 9.

Two limitations of this approach should be noted. First, because $\Pi(k)$ is a nonlinear (triple) product, decomposing $\mathbf{u} = \tilde{\mathbf{u}}_+ + \tilde{\mathbf{u}}_-$ and computing Π_+ and Π_- separately omits the cross-interaction terms between the two truncated fields; consequently, $\Pi_+(k,z) + \Pi_-(k,z)$ equals the full cascade $\Pi(k)$ only at $z = 0$ and $z = H$, and should be interpreted with caution at intermediate altitudes. Second, the hard cutoff $\mathcal{H}_z$ introduces a discontinuity in $\tilde{\mathbf{u}}_\pm$ at $z' = z$; since $\Pi_\pm$ requires spectral differentiation of the truncated field, this discontinuity can introduce spurious high-wavenumber contributions localized near the (moving) cutoff altitude itself, analogous to the periodicity-related caveat already noted for the vertical direction in Section 5.1. Despite these limitations, the decomposition remains useful for identifying the altitudes at which the cascade is most intense.

Figure 15 shows both $\Pi_+(k,z)$ and $\Pi_-(k,z)$ during the upscale cellular growth phase as before. As expected, the full-domain cascade $\Pi(k)$ is recovered at $z = 0$ and $z = H$ respectively (arrows). The direct cascade found at $k > k_H$ (Section 3) is approximately homogeneous with altitude. In contrast, the inverse-cascade signature identified at $k < k_H$ is concentrated either at cloud-top ($\Pi_+(k,z)$) or near the surface ($\Pi_-(k,z)$). This indicates that, within the bulk, the upscale energy transfer is not homogeneous (contrary to the small-scale direct cascade) and that the net inverse transfer close to k_H wavenumbers is concentrated at the near-boundary layers. This is consistent with thermal plumes transporting energy toward the surface and cloud-top boundaries, where it feeds the largest horizontal scales through the (boundary-localized) inverse cascade.

We interpret this as evidence that the upscale growth of the cellular organisation is controlled by a vertical-to-horizontal energy transfer, consistent with the dominant role of the cross-advection term identified in Section 5.2, and physically associated with the horizontal spreading of plume heads as they encounter the stable layers bounding the stratocumulus-topped boundary layer.

6 Discussion

In this work, we seek to clarify the physical drivers underlying the large, quasi-universal aspect ratio of cells in stratocumulus-topped boundary layers (section 2). With the use of the energy cascade methodology (section 3), our results indicate that energy is injected both horizontally, at the cell scale, and vertically, at the scale of individual thermals constrained by the boundary-layer depth. The horizontal injection transfers energy strictly downscale (Section 4), whereas the vertical injection drives a genuine inverse cascade, concentrated near the surface and cloud top (Sections 5). This distinction — between where energy is injected and where it is redistributed upscale — should not be overlooked when interpreting scale-by-scale energy budgets in the atmospheric boundary layer more generally.

Structure functions are commonly used to characterize scale-to-scale energy transfer, and are particularly well suited to airborne measurements, which typically sample wind fields along a single flight track at fixed altitude [e.g. *Brilouet et al.*, 2021]. *Nowak et al.* [2025] recently developed a framework to estimate structure functions and their constitutive terms (buoyancy forcing, dissipation, and transport) for cumulus regimes sampled during the EUREC4A field campaign [*Bony et al.*, 2018]. Consistent with our results, they find that the direction of energy trans-

fer depends strongly on altitude. However, our results also raise a more fundamental concern: structure-function approaches are generally built on an assumption of local isotropy, which our results suggest may not hold in shallow, boundary-confined convection, where vertical–horizontal coupling driven by thermals interacting with their surroundings plays a first-order role. This calls for revisiting the interpretation of turbulence diagnostics in shallow atmospheric boundary layers, as also argued by *Zilitinkevich et al.* [2021] or *DeWitt and Garrett* [2025].

As discussed in the introduction, Rayleigh-Bénard convection offers a useful framework for interpreting the development of large-scale cellular structures [*Celani et al.*, 2010; *Vieweg et al.*, 2021], whose early analyses point to some inverse kinetic-energy cascade as the driver of upscale growth [*Vieweg et al.*, 2022]. Our results are broadly consistent with this picture, although we have less evaluated the corresponding thermal- and buoyancy-variance budgets, whose upscale transfer accompanies the kinetic-energy inverse cascade in classical Rayleigh-Bénard studies and is a natural extension of this work. Our results also align closely with the energy budget of Rayleigh-Bénard superstructures at moderate Rayleigh number reported by *Green et al.* [2020], who find that thermally-driven energy input occurs in the bulk and is subsequently transferred to smaller scales, while vertical energy redistribution by thermal plumes is constrained at the domain walls — inducing lateral spreading of plume heads and a corresponding transfer of energy toward the largest horizontal scales. This is consistent with our truncated-cascade analysis (section 5.3), and suggests that the upscale growth of stratocumulus cells is, at least in part, controlled mechanically by its physical boundaries (the rigid surface and the strong density inversion at cloud top) rather than solely by radiative or microphysical processes. We do not, however, interpret this as evidence that phase change and radiative heterogeneities are unimportant: our own results suggest that these processes instead set the horizontal injection scale and its slow evolution, while the boundary-confined mechanism identified here governs the subsequent inverse-cascade transfer of energy to larger scales. Disentangling the relative roles of these two, likely complementary, pathways is an important target for future work ; for instance by tracking the behavior of individual plumes through object-oriented characterization [*Brient et al.*, 2024] as they approach and interact with the boundary-layer top and surface.

Several limitations and further considerations regarding the present study could be addressed in future work on more realistic geophysical flows. First, our low- and high-resolution simulations saturate at different aspect ratios (30–40 versus ≈20, respectively), and even the larger of our two domains has a relatively modest aspect ratio ($\Gamma_{\text{domain}} \approx 150$); given that upscale cascades in confined turbulence are known to saturate once they reach the domain scale [*Vieweg et al.*, 2021], larger-domain simulations are needed to confirm that the aspect ratios reported here reflect a genuine physical equilibrium rather than a finite-domain, double-periodicity artifact. Second, our setup imposes a constant geostrophic wind (needed for calculating interactive surface fluxes), and a roll-like alignment of cells with the mean wind emerges after about 24 hours (Section 2). This suggests that shear may interact with, and potentially limit, the upscale growth mechanism identified here and should be analyzed more deeply. Third, precipitation was disabled in our simulations in order to isolate and analyze the role of the dynamics. Since drizzle is a known driver of the transition to open-cell convection [*Wood*, 2012; *Mayer et al.*, 2026], its interaction with the boundary-confined inverse-cascade mechanism proposed here remains to be characterized. Finally, we note that this mechanism — energy injection at a boundary-confined plume scale, followed by upscale transfer sustained by confinement at rigid or quasi-rigid boundaries — is not obviously specific to stratocumulus, and may extend to other boundary-confined convective systems as suggested by the slight cellular increase seen in the dry convective boundary layer [*Jonker et al.*, 1999; *de Roode et al.*, 2004]. It can also help understanding other geophysical convective-driven organized flows, such as Jovian vortices [*Siegelman et al.*, 2022], and potentially to non-atmospheric analogues such as solar supergranulation [*Rincon and Rieutord*, 2018]. Testing this more general hypothesis, together with an observational validation of the mechanism itself — for instance using satellite-based cell-tracking algorithms to relate cell growth rates to boundary-layer decoupling state — offers a promising avenue for future research.

7 Conclusions

In this study, we simulate the diurnal cycle of a stratocumulus-topped boundary layer using large-eddy simulations performed with the Meso-NH model, with the aim of interpreting the upscale growth of the cellular pattern. Because this growth is associated with the aggregation of variance and energy at the largest scales, we investigate whether an inverse cascade transfers energy from the scales of energy injection to the largest scales. Following the methodology of *Alexakis et al.* [2024], we find that energy is mostly injected by thermal plumes constrained by the boundary-layer depth, and that it is transferred to the largest scales ($L > \mathsf{H}$) through the advection of horizontal winds by vertical motions. At nighttime, a second cross-advection cascade – horizontal motions advecting vertical velocity – also transfer energy upscale. During daytime, when boundary-layer decoupling reduces this transfer, this term become positive (downscale energy transfer) but the horizontal field partly compensates through its own self-interaction, which help sustain the growth of the existing cellular pattern. Finally, our results suggest that these energy transfers are particularly prominent near the vertical boundaries, suggesting that these boundaries play an important role.

This study shows that the upscale mechanisms in the stratocumulus-topped boundary layer are similar to those identified for superstructures in Rayleigh–Bénard convection in high-resolution simulations. This suggests that, to first order, moisture-related processes are not essential for upscale transfers, which instead rely on nonlinear kinetic energy transfers. This study also highlights the importance of inverse energy cascades, as in two-dimensional turbulence, and suggests revisiting the concept of isotropic turbulence in atmospheric boundary layers, in line with *Zilitinkevich et al.* [2021]. Diabatic processes may nevertheless play a non-negligible role in the cellular appearance, through the decoupling and aggregation of plumes. Finally, observations show a constant cell size [*Monnier et al.*, 2026], which raises the question of what stops the inverse cascade and upscale cellular growth. This points to a potential large-scale drag setting the scale at which the cascade stops, possibly associated with humidity–radiation effects constrained by the diurnal cycle. Following recent studies on cumulus clouds [*Bony et al.*, 2025; *Falcone et al.*, 2026], further analyses should focus on plume–plume and plume–environment interactions in both well-mixed and decoupled shallow atmospheric layers.

Acknowlegedments

This work was supported by the French ANR grant MOBYDYC (ANR-22-CE01-0005). FB supports the Institut Universitaire de France for financial support and BP acknowledges the Ecole Normale Supérieure for funding his PhD fellowship. The authors would like to thank Lokahith Agasthya, Alexandros Alexakis, Robin Hogan, Louis Jaffeux, Martin Janssens, Brian Mapes, Jakub Nowak, Olivier Pauluis for valuable discussions. This work was granted access to the HPC resources of IDRIS made by GENCI (Jean Zay supercomputer). The authors gratefully acknowledge the Meso-NH support team (LAERO/CNRM) for their technical assistance and valuable help with the model setup and simulations.

References

Agasthya, L., C. Muller, and M. Cheve (2025), Moist convective scaling: insights from an idealised model, *Quart. J. Roy. Meteor. Soc.*, *151*, e4902, doi:10.1002/qj.4902.

Agee, E. M., T. Chen, and K. Dowell (1973), A review of mesoscale cellular convection, *Bull. Amer. Meteor. Soc.*, *54*(10), 1004–1012.

Ahlers, G., S. Grossmann, and D. Lohse (2009), Heat transfer and large scale dynamics in turbulent rayleigh-bénard convection, *Reviews of modern physics*, *81*(2), 503.

Alexakis, A., and L. Biferale (2018), Cascades and transitions in turbulent flows, *Physics Reports*, *767*, 1–101.

Alexakis, A., R. Marino, P. D. Mininni, A. van Kan, R. Foldes, and F. Feraco (2024), Large-scale self-organization in dry turbulent atmospheres, *Science*, *383*(6686), 1005–1009.

Atkinson, B., and J. Wu Zhang (1996), Mesoscale shallow convection in the atmosphere, *Reviews of Geophysics*, *34*(4), 403–431.

Batchelor, G. K. (1969), Computation of the energy spectrum in homogeneous two-dimensional turbulence, *The Physics of Fluids*, *12*(12), II–233.

Bony, S., B. Stevens, F. Ament, S. Bigorre, P. Chazette, S. Crewell, J. Delanoë, K. Emanuel, D. Farrell, C. Flamant, et al. (2018), Eurec4a: A field campaign to elucidate the couplings between clouds, convection and circulation, in *Shallow Clouds, Water Vapor, Circulation, and Climate Sensitivity*, pp. 357–396, Springer.

Bony, S., B. Poujol, B. Mckim, N. Rochetin, M. Lothon, J. Windmiller, N. Maury, C. Dufaux, L. Jaffeux, P. Chazette, et al. (2025), Evidence for the role of thermal and cloud merging in mesoscale convective organization, *Atmos. Chem. Phys.*, *25*(23), 17,331–17,362.

Bretherton, C. S., and M. Wyant (1997), Moisture transport, lower-tropospheric stability, and decoupling of cloud-topped boundary layers, *J. Atmos. Sci.*, *54*(1), 148–167.

Brient, F., F. Couvreux, C. Rio, and R. Honnert (2024), Coherent subsiding structures in large-eddy simulations of atmospheric boundary layers, *Quart. J. Roy. Meteor. Soc.*, *150*(759), 834–856.

Brilouet, P.-E., M. Lothon, J.-C. Etienne, P. Richard, S. Bony, J. Lernoult, H. Bellec, G. Vergez, T. Perrin, J. Delanoë, et al. (2021), The eurec 4 a turbulence dataset derived from the safire atr 42 aircraft, *Earth System Science Data*, *13*(7), 3379–3398.

Celani, A., S. Musacchio, and D. Vincenzi (2010), Turbulence in more than two and less than three dimensions, *Physical review letters*, *104*(18), 184,506.

Cieszelski, R. (1998), A case study of rayleigh-bénard convection with clouds, *Bound. Lay. Meteor.*, *88*(2), 211–237.

de Roode, S. R., P. G. Duynkerke, and H. J. Jonker (2004), Large-eddy simulation: How large is large enough?, *J. Atmos. Sci.*, *61*(4), 403–421.

DeWitt, T. D., and T. J. Garrett (2025), Global sonde datasets do not support a mesoscale transition in the turbulent energy cascade, arXiv:2510.23625, doi:10.48550/arXiv.2510.23625.

Duynkerke, P. G., S. R. de Roode, M. C. van Zanten, J. Calvo, J. Cuxart, S. Cheinet, A. Chlond, H. Grenier, P. J. Jonker, M. Köhler, et al. (2004), Observations and numerical simulations of the diurnal cycle of the eurocs stratocumulus case, *Quart. J. Roy. Meteor. Soc.*, *130*(604), 3269–3296.

Falcone, D. P., M. R. Igel, and J. A. Biello (2026), Idealised cumulus cloud-scale motions and the dynamics of isolated and coupled flows, *Geophysical & Astrophysical Fluid Dynamics*, *120*(3), 301–328, doi:10.1080/03091929.2026.2682659.

Feingold, G., I. Koren, H. Wang, H. Xue, and W. A. Brewer (2010), Precipitation-generated oscillations in open cellular cloud fields, *Nature*, *466*(7308), 849.

Fiedler, B. H. (1985), Mesoscale cellular convection: is it convection?, *Tellus A*, *37*(2), 163–175.

Frisch, U. (1995), *Turbulence: The Legacy of A. N. Kolmogorov*, Cambridge University Press.

Garay, M. J., R. Davies, C. Averill, and J. A. Westphal (2004), Actinoform clouds: Overlooked examples of cloud self-organization at the mesoscale, *Bulletin of the American Meteorological Society*, *85*(10), 1585–1594.

Geoffroy, O., J.-L. Brenguier, and F. Burnet (2010), Parametric representation of the cloud droplet spectra for les warm bulk microphysical schemes, *Atmos. Chem. Phys.*, *10*(10), 4835–4848.

Glassmeier, F., and G. Feingold (2017), Network approach to patterns in stratocumulus clouds, *Proc. Nat. Ac. Sci.*, p. 201706495.

Green, G., D. G. Vlaykov, J. P. Mellado, and M. Wilczek (2020), Resolved energy budget of superstructures in rayleigh–bénard convection, *Journal of Fluid Mechanics*, *887*, A21.

Gregory, D., J.-J. Morcrette, C. Jakob, A. Beljaars, and T. Stockdale (2000), Revision of convection, radiation and cloud schemes in the ecmwf integrated forecasting system, *Quart. J.*

Roy. Meteor. Soc., *126*(566), 1685–1710.

Jonker, H. J. J., P. G. Duynkerke, and J. W. M. Cuijpers (1999), Mesoscale fluctuations in scalars generated by boundary layer convection, *J. Atmos. Sci.*, *56*(5), 801–808, doi: 10.1175/1520-0469(1999)056⟨0801:MFISGB⟩2.0.CO;2.

Kazil, J., T. Yamaguchi, and G. Feingold (2017), Mesoscale organization, entrainment, and the properties of a closed-cell stratocumulus cloud, *Journal of Advances in Modeling Earth Systems*, *9*, 2214–2229, doi:10.1002/2017MS001072.

Khairoutdinov, M., and Y. Kogan (2000), A new cloud physics parameterization in a large-eddy simulation model of marine stratocumulus, *Mon Weather Rev*, *128*(1), 229–243.

Kraichnan, R. H. (1967), Inertial ranges in two-dimensional turbulence, *Tech. rep.*

Krishnamurti, R. (1975), On cellular cloud patterns. part 1: Mathematical model, *Journal of Atmospheric Sciences*, *32*(7), 1353–1363.

Krueger, A. F., and S. Fritz (1961), Cellular cloud patterns revealed by tiros i, *Tellus*, *13*(1), 1–7, doi:10.1111/j.2153-3490.1961.tb00061.x.

Lac, C., P. Chaboureau, V. Masson, P. Pinty, P. Tulet, J. Escobar, M. Leriche, C. Barthe, B. Aouizerats, C. Augros, et al. (2018), Overview of the meso-nh model version 5.4 and its applications, *Geosci. Model Dev. Discuss.*, pp. 1929–1969.

Lareau, N. P., Y. Zhang, and S. A. Klein (2018), Observed boundary layer controls on shallow cumulus at the arm southern great plains site, *J. Atmos. Sci.*, *75*(7), 2235–2255.

Leith, C. E. (1968), Diffusion approximation for two-dimensional turbulence, *Physics of Fluids*, *11*(3), 671–672.

Masson, V., P. Le Moigne, E. Martin, S. Faroux, A. Alias, R. Alkama, S. Belamari, A. Barbu, A. Boone, F. Bouyssel, et al. (2013), The surfexv7. 2 land and ocean surface platform for coupled or offline simulation of earth surface variables and fluxes, *Geoscientific Model Development*, *6*(4), 929–960.

Mayer, J., D. Gasbarra, R. J. Hogan, E. Malina, S. L. Mason, and B. Piskala Gvozdikova (2026), Earthcare reveals details on the role of rain in closed-to-open cell transitions, *Atmos. Chem. Phys.*, *26*(19), 14,085–14,110, doi:10.5194/acp-26-14085-2026.

Monnier, E., F. Brient, and J.-L. Dufresne (2026), Diurnal cycle of stratocumuli mesoscale convective cells in the south-east pacific, *EGUsphere*, *2026*, 1–35.

Muller, C., and S. Bony (2015), What favors convective aggregation and why?, *Geophys Res Lett*, *42*(13), 5626–5634.

Nowak, J. L., M. Wac lawczyk, J. C. Vassilicos, S. Król, and S. P. Malinowski (2025), Scale-by-scale budget of turbulence kinetic energy in the convective atmospheric boundary layer: Analysis of structure functions, *Quart. J. Roy. Meteor. Soc.*, *151*(767), e4879.

Ouyang, X., B. Zhou, H. Wang, H. Xiao, K. Huang, and M. Wang (2026), On the cell broadening of mesoscale cellular convection in a well-mixed boundary layer, *J. Adv. Model. Earth Syst.*, *18*(7), e2025MS005,576.

Pandey, A., J. D. Scheel, and J. Schumacher (2018), Turbulent superstructures in rayleigh-bénard convection, *Nature Communications*, *9*, 2118, doi:10.1038/s41467-018-04478-0.

Pauluis, O., and J. Schumacher (2011), Self-aggregation of clouds in conditionally unstable moist convection, *Proc. Nat. Ac. Sci.*, *108*(31), 12,623–12,628, doi:10.1073/pnas.1102339108.

Poujol, B., A. van Kan, and A. Alexakis (2020), Role of the forcing dimensionality in thin-layer turbulent energy cascades, *Physical Review Fluids*, *5*(6), 064,610.

Rémillard, J., P. Kollias, E. Luke, and R. Wood (2012), Marine boundary layer cloud observations in the azores, *J Clim*, *25*(21), 7381–7398.

Rincon, F., and M. Rieutord (2018), The sun's supergranulation, *Living Reviews in Solar Physics*, *15*(1), 6.

Schmidt, G., J. Annan, P. Bartlein, B. Cook, É. Guilyardi, J. Hargreaves, S. Harrison, M. Kageyama, A. LeGrande, B. Konecky, et al. (2013), Using palaeo-climate comparisons to constrain future projections in cmip5, *Climate of the Past*, *10*(1), 221–250.

Siegelman, L., P. Klein, A. P. Ingersoll, S. P. Ewald, W. R. Young, A. Bracco, A. Mura, A. Adriani, D. Grassi, C. Plainaki, et al. (2022), Moist convection drives an upscale energy

transfer at jovian high latitudes, *Nature Physics*, *18*(3), 357–361.

Stevens, B., S. Bony, H. Brogniez, L. Hentgen, C. Hohenegger, C. Kiemle, T. S. L'Ecuyer, A. K. Naumann, H. Schulz, P. A. Siebesma, et al. (2020), Sugar, gravel, fish and flowers: Mesoscale cloud patterns in the trade winds, *Quart. J. Roy. Meteor. Soc.*, *146*(726), 141–152.

Stull, R. B. (1988), *An introduction to boundary layer meteorology*, Springer Science & Business Media.

Vieweg, P. P., J. D. Scheel, and J. Schumacher (2021), Supergranule aggregation for constant heat flux-driven turbulent convection, *Physical review research*, *3*(1), 013,231.

Vieweg, P. P., J. D. Scheel, R. Stepanov, and J. Schumacher (2022), Inverse cascades of kinetic energy and thermal variance in three-dimensional horizontally extended turbulent convection, *Physical review research*, *4*(4), 043,098.

Wood, R. (2012), Stratocumulus clouds, *Mon Weather Rev*, *140*(8), 2373–2423.

Wood, R., and D. L. Hartmann (2006), Spatial variability of liquid water path in marine low cloud: The importance of mesoscale cellular convection, *J Clim*, *19*(9), 1748–1764.

Zhou, X., and C. S. Bretherton (2019), Simulation of mesoscale cellular convection in marine stratocumulus: 2. nondrizzling conditions, *J. Adv. Model. Earth Syst.*, *11*(1), 3–18.

Zhou, X., C. Zhang, Z. Xiao, Y. Li, and G. Lu (2025), Inverse energy cascades in the boundary layer during strong winds based on doppler lidar, *Geophysical Research Letters*, *52*(2), e2024GL113,273.

Zilitinkevich, S., E. Kadantsev, I. Repina, E. Mortikov, and A. Glazunov (2021), Order out of chaos: Shifting paradigm of convective turbulence, *J. Atmos. Sci.*, *78*(12), 3925–3932.

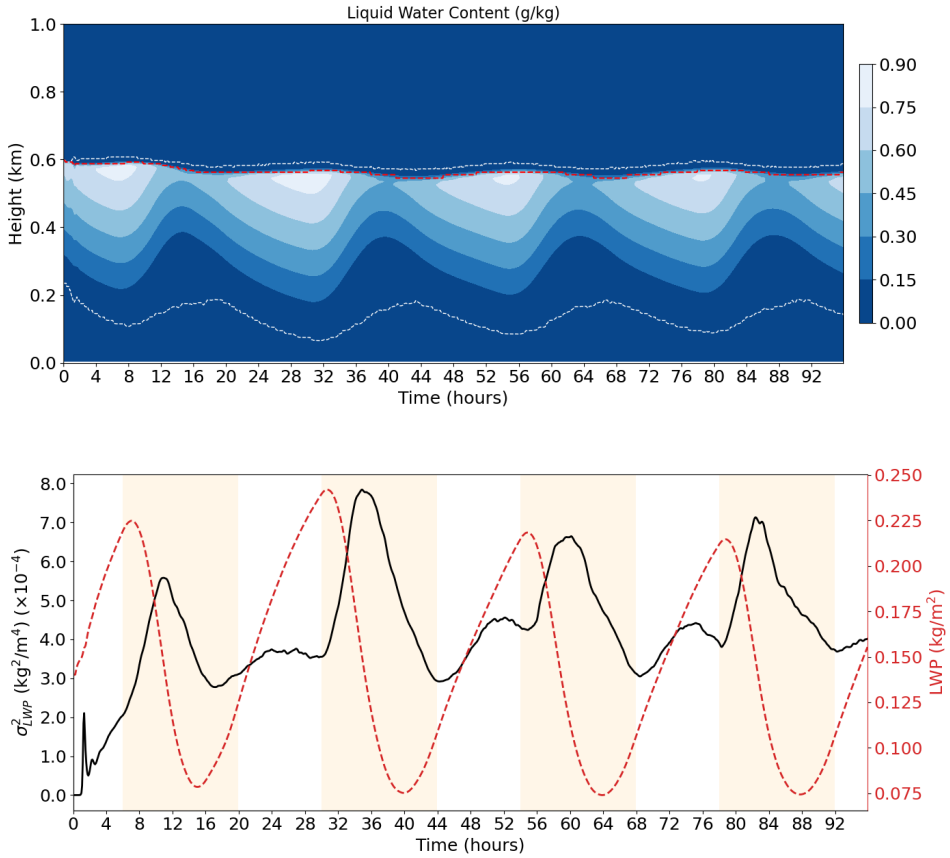


Figure 1: (Top) Evolution of the liquid water content (g/kg) for the LR simulation. White and red lines show the minimum cloud fraction (defined when the domain average is higher than 0.01) and the boundary-layer depth respectively. (Bottom) Evolution of the mean and variance of Liquid Water Path (red and black respectively). The yellow bands show daytime.

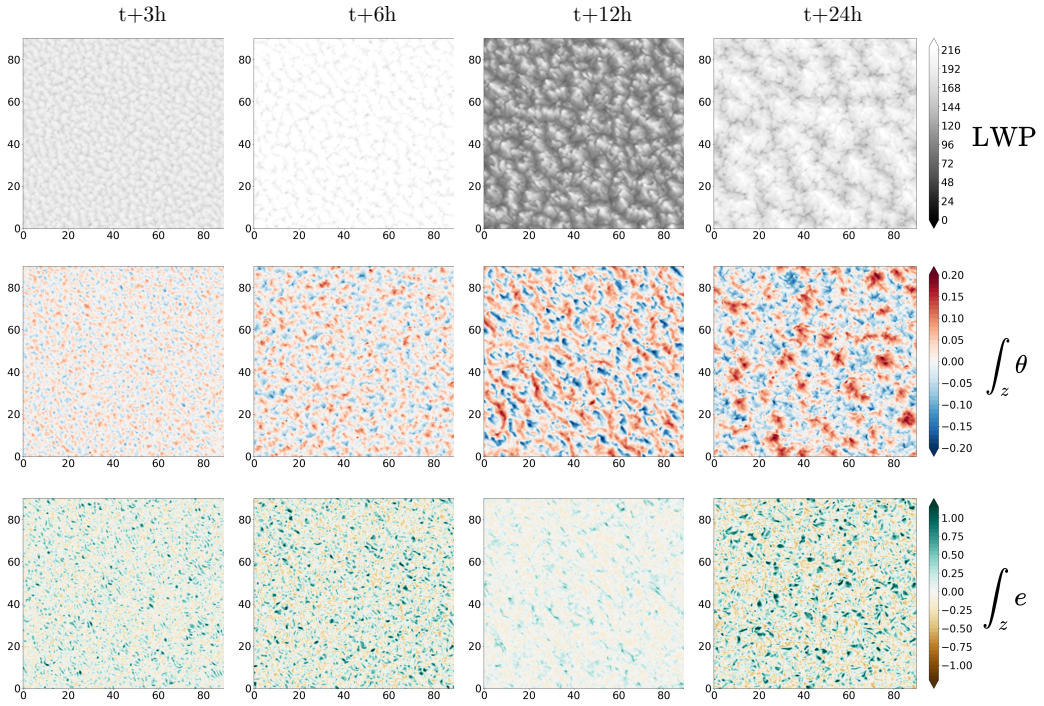


Figure 2: Spatial distribution of Liquid Water Path (g/m^2) and anomalies of vertically-averaged liquid-water potential temperature ($\theta_l^{'}$ - K) and of Turbulent Kinetic Energy (TKE - m^2/s^2) at t+3, t+6, t+12, t+24 for the LR simulation.

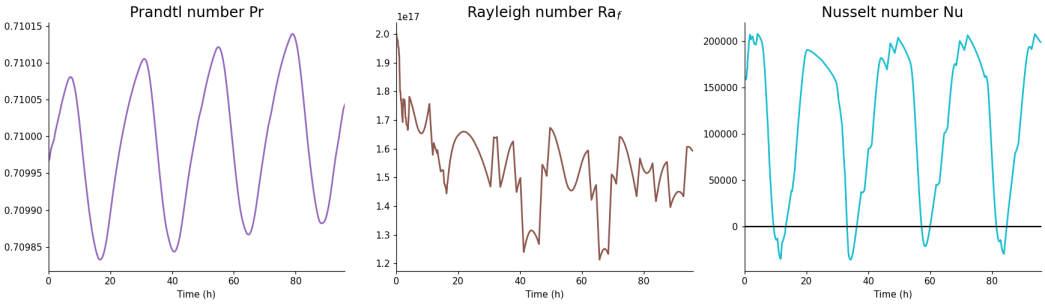


Figure 3: Evolution in time of adimensional Prandtl, Rayleigh and Nusselt numbers respectively for the LR simulation. Note that Rayleigh number are on the order of 10^{17}.

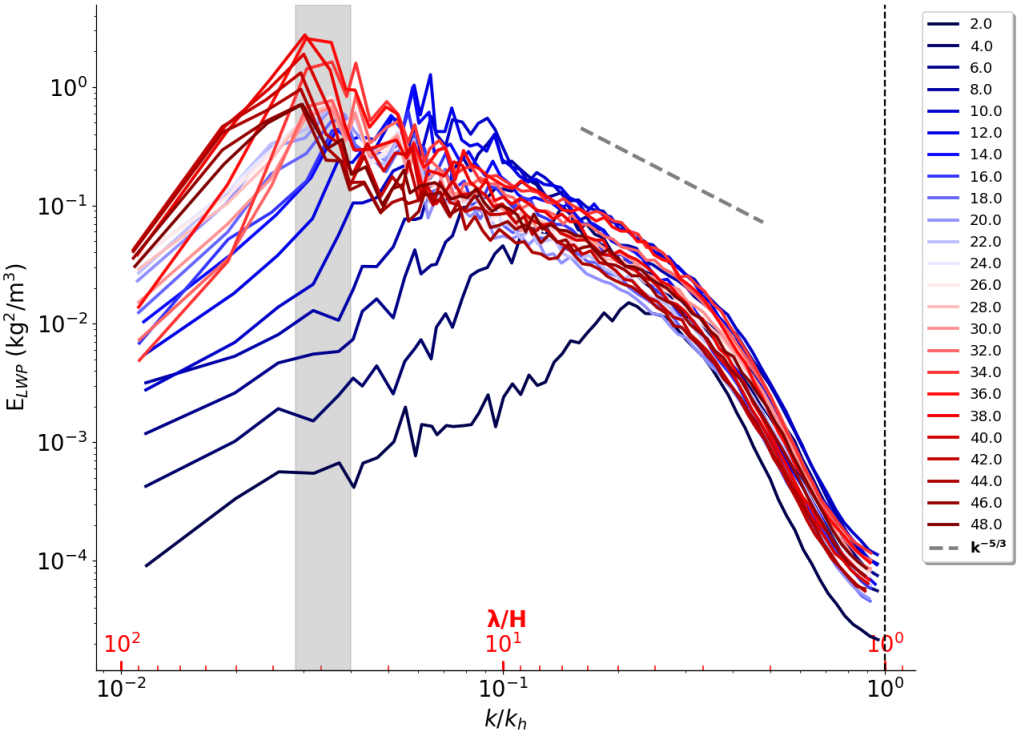


Figure 4: Radial spectra of the Liquid Water Path variance (kg^2/m^3) for the first 48 hours of the LR simulation. Wavenumbers are divided by k_{H}, the wavenumber corresponding to the boundary-layer depth H (vertical dashed line). Observations of Γ_{LWP} are shown with a grey bar. The -5/3 line is shown as a dashed grey line.

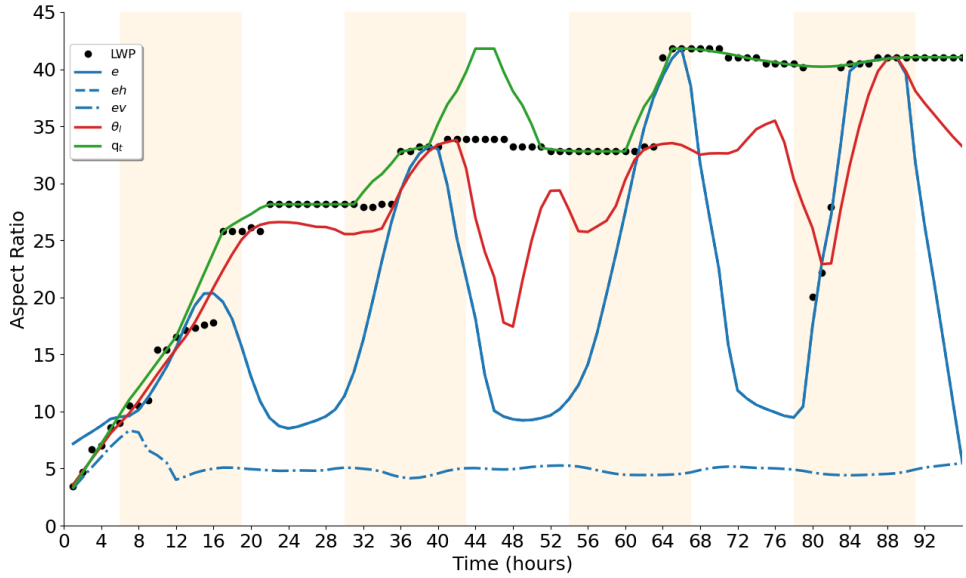


Figure 5: Temporal evolution for the LR simulation of the aspect ratio of Liquid Water Path (black dots), and the vertical-averaged Turbulent Kinetic Energy (blue), liquid water potential temperature (red) and total specific humidity (green). The TKE is separated in their horizontal (dashed) and vertical (dotted-dashed) components. The horizontal component is hidden by the full TKE line. The lines show lowess regression applied to the raw data with a smoothing parameter of 10 hours (≈10%) to reduce high-frequency fluctuations.

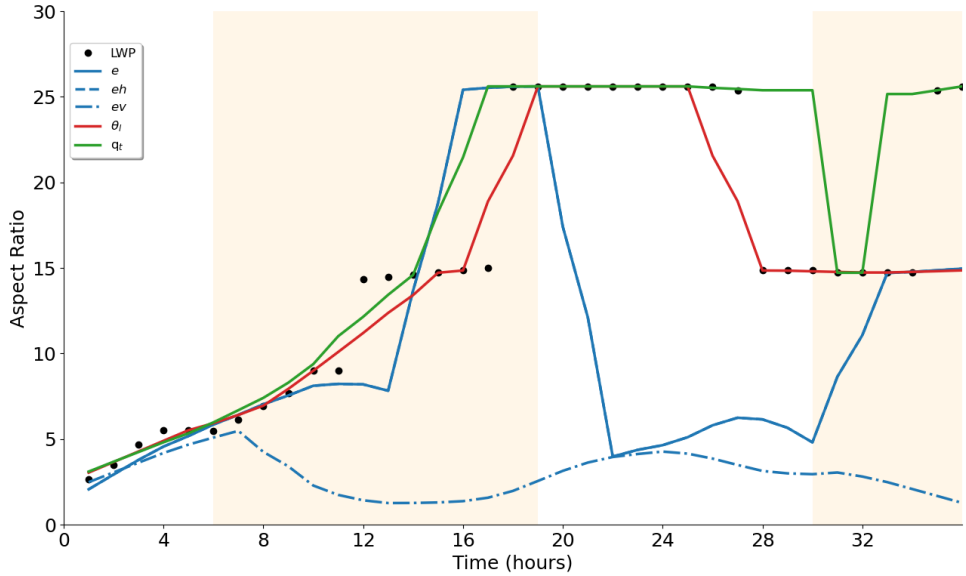


Figure 6: Same as figure 5 for the HR simulation during 36 hours. Lines are colors are defined on figure 5.

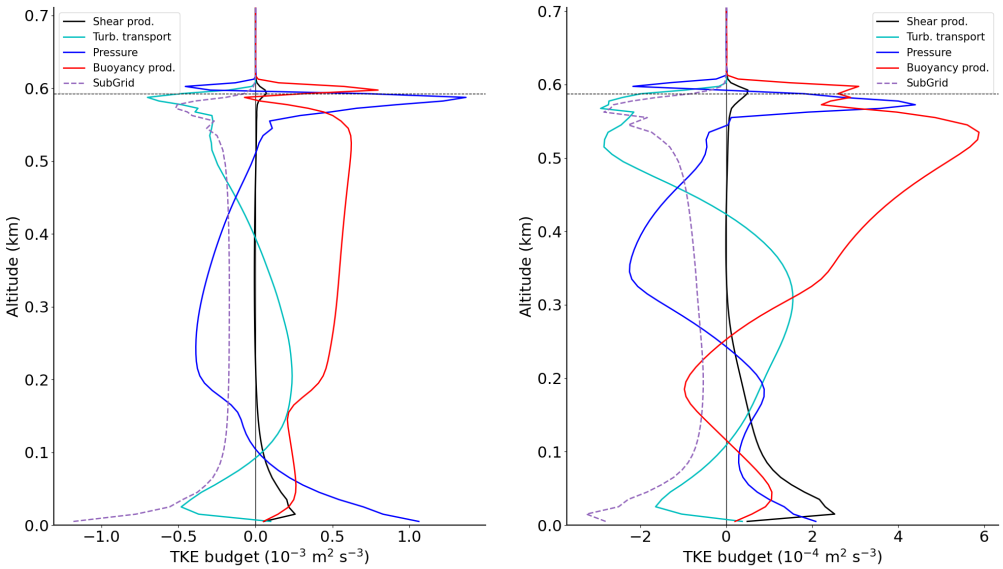


Figure 7: Decomposition of the domain-averaged TKE budget of the HR simulation at nighttime (left, t=6±3 hours) and daytime (right, t=12±3 hours). Resolved parts are represented as full lines and the subgrid component, mostly linked to dissipation, as a dashed line.

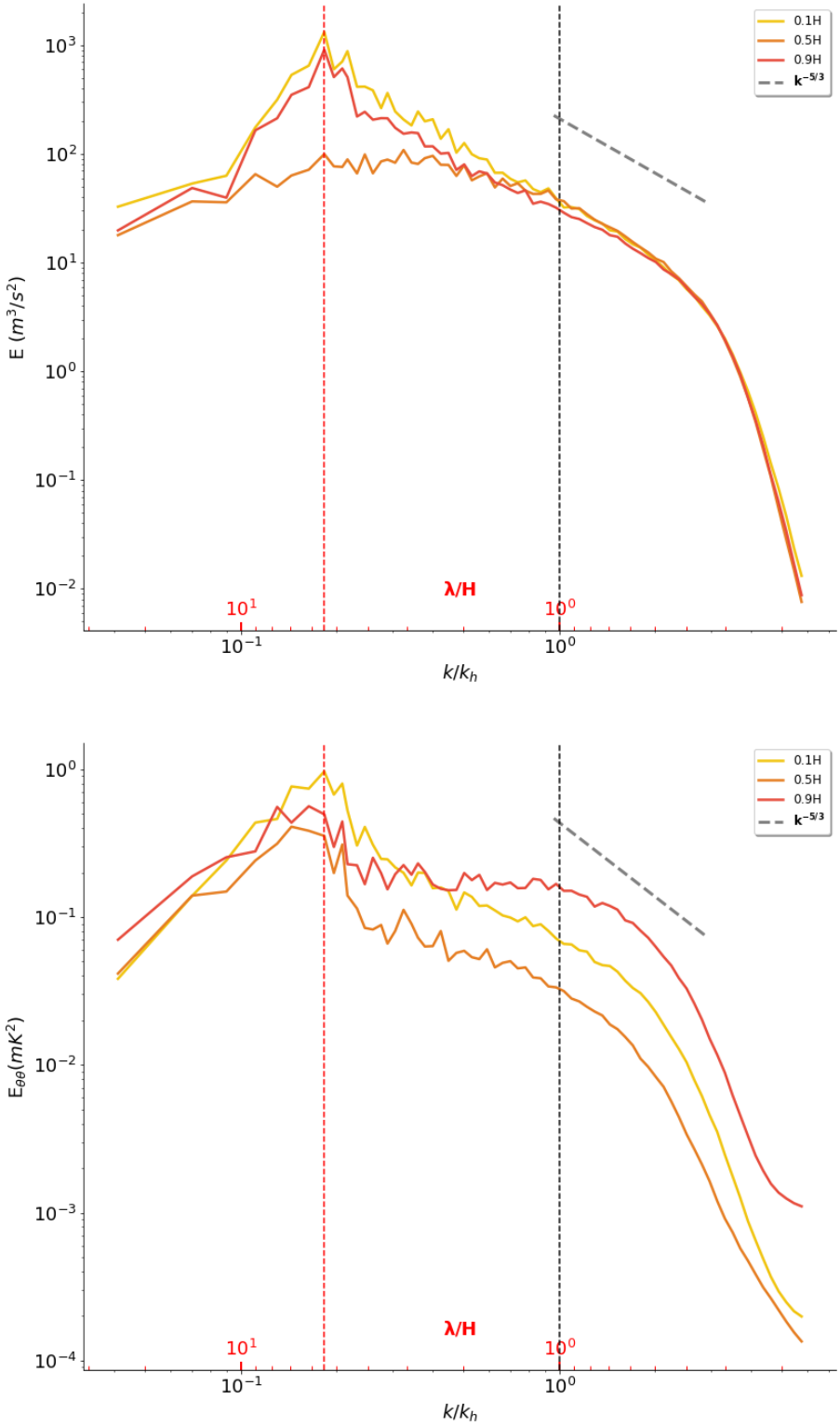


Figure 8: Radial spectra of turbulent kinetic energy E (m^3/s^2) and liquid-water potential temperature variance $E_{\theta\theta}$ ($m.K^2$) for the HR simulation at t+6h. Each spectrum is an vertical averaging over a 0.2 H depth (≈120 m) at altitudes of 0.1, 0.5 and 0.9 H. Wavenumbers are divided by the boundary-layer depth (vertical dashed line). Aspect ratio Γ_{LWP} is shown as the red dashed vertical line. The -5/3 line is shown as the dashed grey line in the energy spectrum.

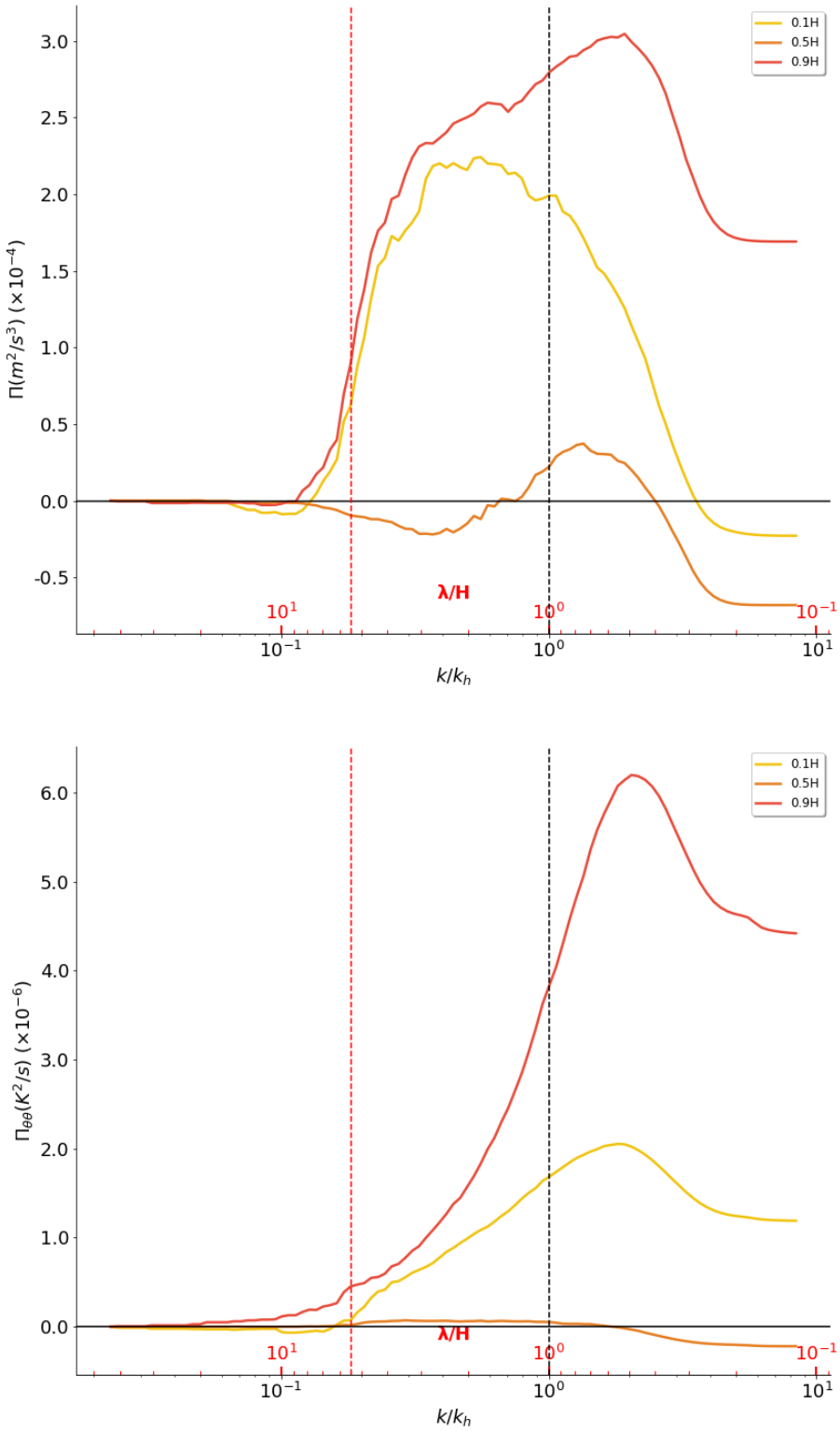


Figure 9: Energy cascade Π (m^2/s^3) and thermal variance cascade $\Pi_{\theta\theta}$ (K^2/s) at different altitudes for the HR simulation at t+6h. Colors and lines are defined on figure 8

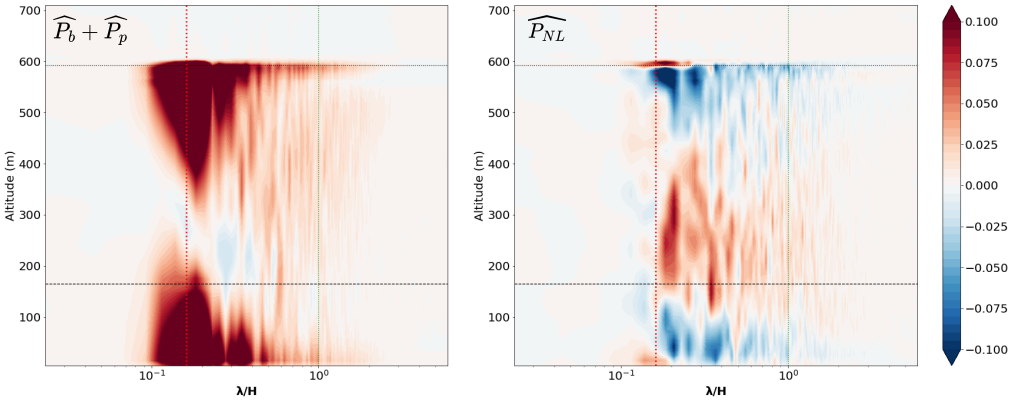


Figure 10: Component of the TKE budget in the Fourier space (m^3/s^3) computed horizontally at each altitude for the HR simulation at t+6h. Left panel represents the sum of buoyancy production and pressure redistribution, and right panel shows the non-linear transport. The horizontal dashed line is the domain-mean cloud base and the red line is the cellular aspect ratio. Dotted lines shows the boundary layer height H.

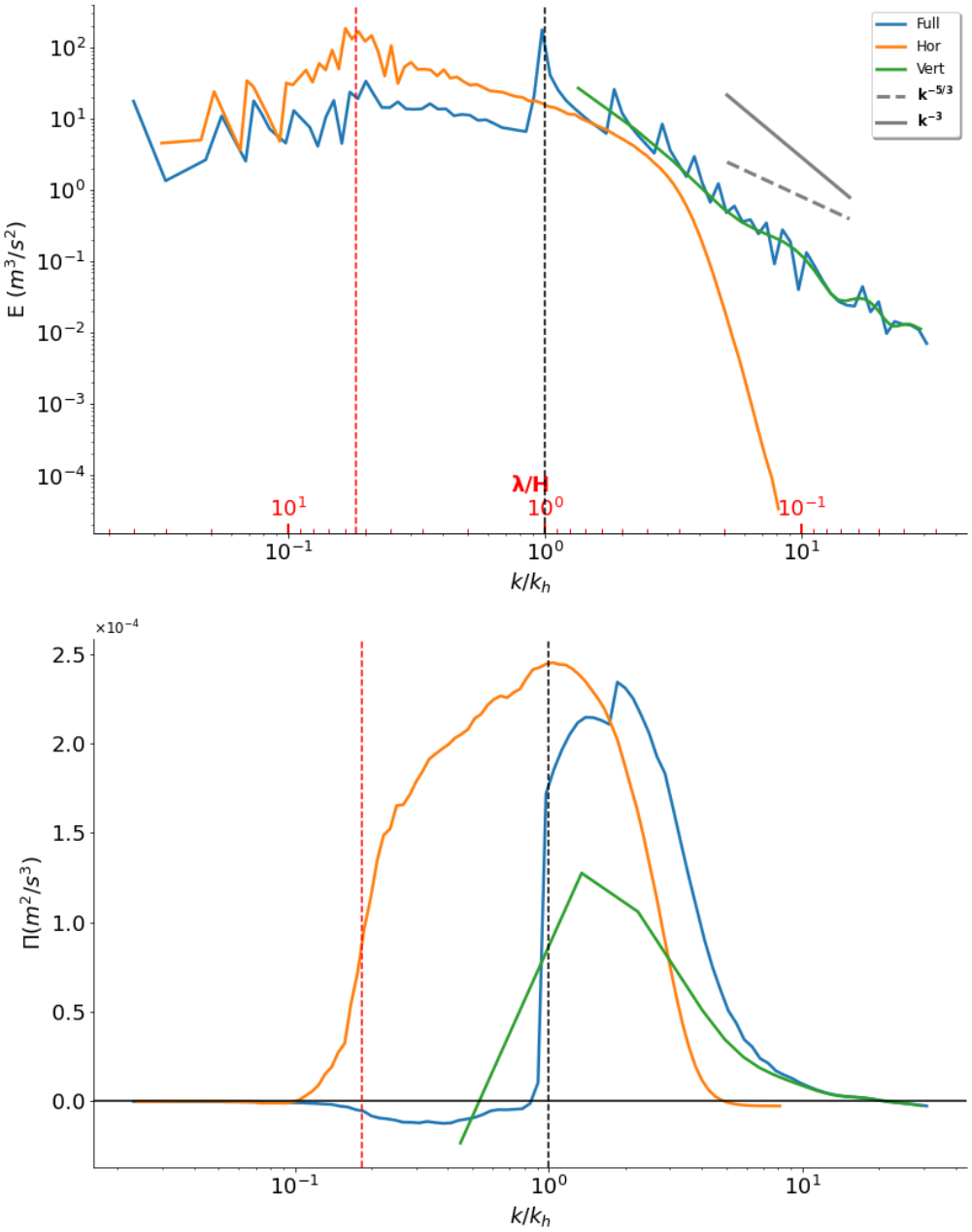


Figure 11: Full (blue), horizontal (orange), and vertical (green) energy spectra E (top) and cascade Π (bottom) for the HR simulation at t+6h. The aspect ratio Γ_{LWP} is represented by the vertical dashed red line.

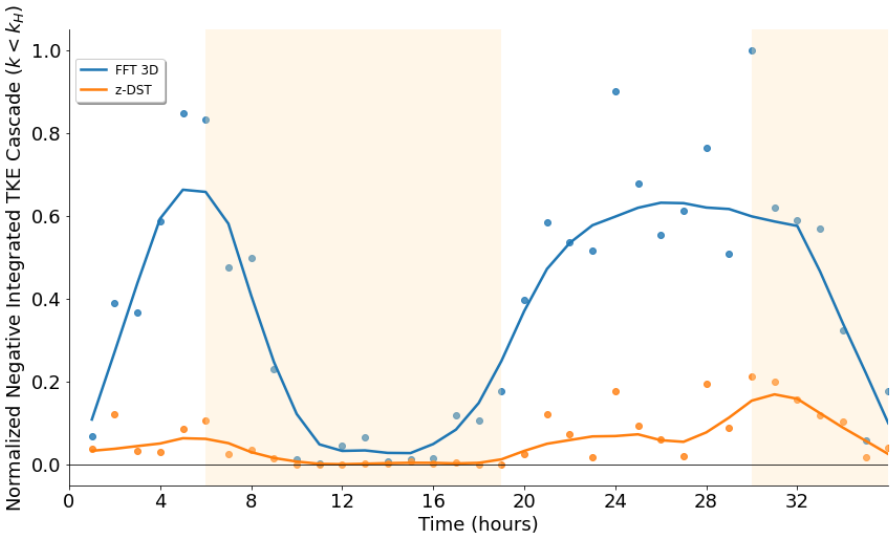


Figure 12: Evolution in time of the integrate of the negative TKE cascade for wavenumbers lower than k_H for the HR simulation. Lines show Lowess regressions applied to the hourly raw data (dots) with a smoothing parameter of 7.2 hours (20%). Blue correspond to the 3D FFT computation and orange to the Discrete Sine Transform (DST) transforms along the z axis. Both variables are plot relative to the maximum absolute value of the TKE cascade.

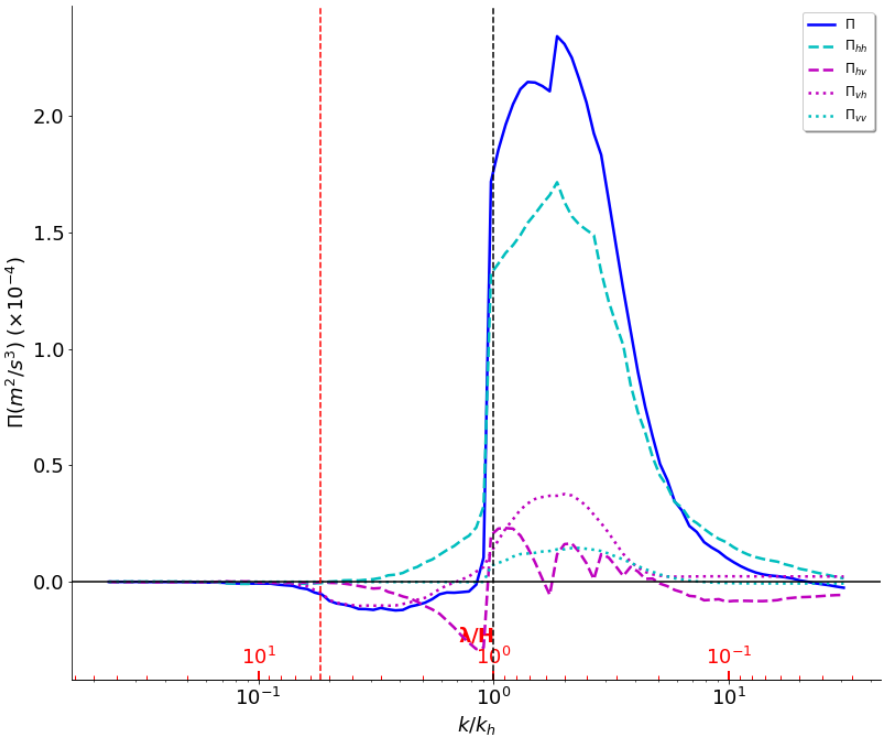


Figure 13: Separation of the spherically-averaged cascade shown on figure 11 (blue line) between isotropic (cyan) and anistropic (magenta) terms for the HR simulation at t+6h. The aspect ratio of the LWP cells is represented by the vertical dashed red line.

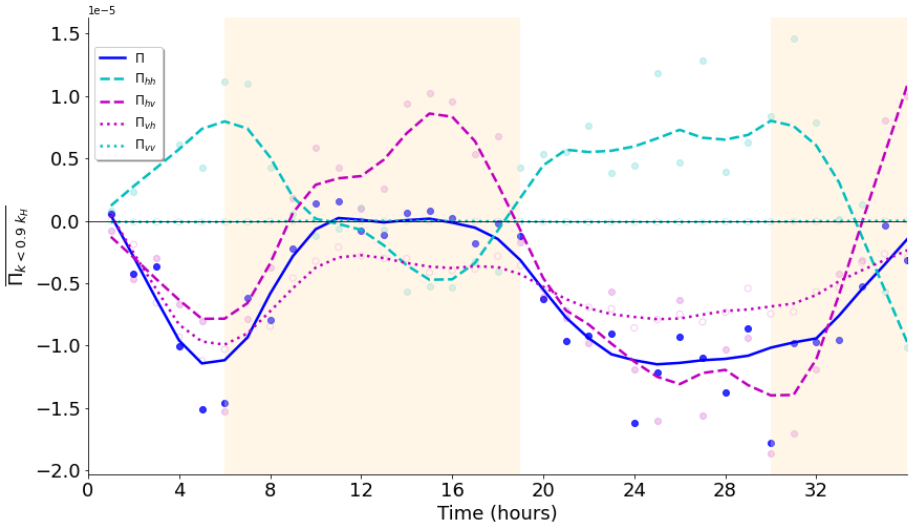


Figure 14: Evolution of time of the integrate of the cascades for all $k<0.9\,k_H$ separated in isotropic and cross-advection terms for the HR simulation. Lowess regression (curves) applied to the hourly raw data (dots) with a smoothing parameter of 7.2 hours (20%).

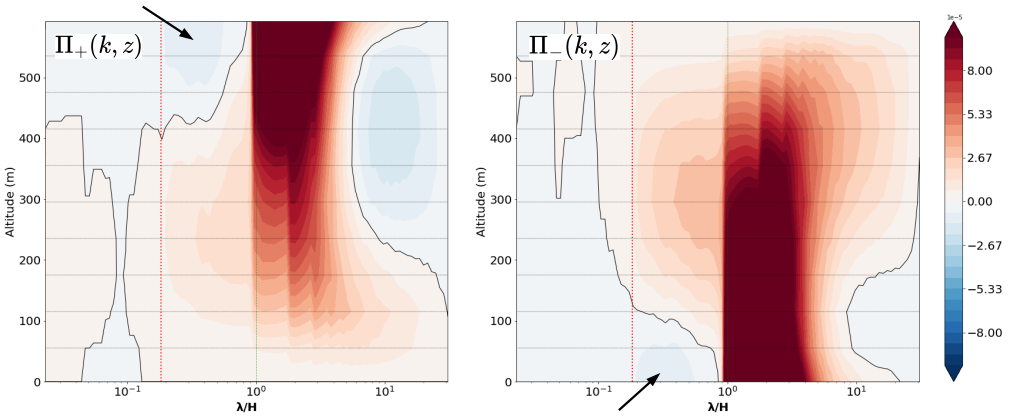


Figure 15: Bottom-up and top-down truncated energy cascade (Π_+ and Π_- respectively) for the HR simulation at t=6h. The zero-line is shown with a black line. Arrows highlights the negative cascade at $k<k_H$. Horizontal dashed line represented discretized levels used to calculated truncated cascades.